DISSERTATION

UNCOVERING DETAILS OF THE ELECTRICAL PROPERTIES OF CELLS

Submitted by

Jasmine E. Nejad

School of Biomedical Engineering

In partial fulfillment of the requirements

For the Degree of Doctor of Philosophy

Colorado State University

Fort Collins, Colorado

Fall 2022

Doctoral Committee:

Advisor: Kevin L. Lear

Stuart Tobet
Ashley K. McGrew
Steve Simske

ABSTRACT

UNCOVERING DETAILS OF THE ELECTRICAL PROPERTIES OF CELLS

The electrical properties of cells have long been studied by scientists across many fields, yet there are still major gaps in our understanding of the intrinsic properties of many types of cells, such as parasite eggs, as well as the detailed electrical behavior of excitable

cells, such as neurons. This work aims to provide insights into how these properties can be measured and how machine learning can be used to advance our understanding of these phenomena.

The first part of this work discusses the development of a microfluidic impedance cytometer for the enumeration and classification of parasite eggs isolated from fecal samples. Current diagnostics in parasitology rely on the manual counting of eggs, cysts, and oocysts on microscope slides that have been isolated from fecal samples. These methods depend on trained technicians with expertise in the preparation of samples and detection of parasites on these slides, which increases cost and turnaround times for diagnosis. This leads many farmers and ranchers to opt to pool fecal samples from multiple animals to save time and labor. In cattle herds, resistance is often due to underdosing, which can be caused by treating all animals to an average weight or treating by the calendar instead of targeted deworming. This blanket use of anthelmintics, or anti-parasitic medication, is leading to concerns about anthelmintic resistance, which would cause major issues in the livestock industry, as well create unforeseen ecological imbalances. The developed microfluidic system provides a proof-of-concept for a microfluidic impedance cytometer capable of measuring the impedance of parasite eggs at multiple

frequencies, simultaneously, as each of the eggs passes through a microfluidic channel past a sensing region. This region consists of parallel electrodes on the top and bottom of the channel, allowing for measurement of the voltage across the channel. When an egg passes through, the signal is interrupted, leaving a distinct profile of the electrical properties at each frequency over time. This system shows proof-of-concept of the impedance measurements at 500kHz and 10MHz and provides insights for further exploration of these properties, with the eventual use of machine learning algorithms for discrimination of parasite eggs from debris, and differentiation of parasite genera.

The second part of this work discusses machine learning classification of neuronal subtypes based on features extracted from patch-clamp recordings from adult mice, using data acquired from publicly available databases. Classification of neuronal subtypes has been a continuously progressing area of neuroscience, building on advancements in our understanding of the morphology, physiology, and biochemistry of different neurons, and contributing to the accuracy and repeatability of action potential and neuronal circuit models. This work explores the use of k-nearest neighbors, support vector machine, decision tree, logistic regression, and naïve Bayes algorithms for classification of fast-spiking or regular-spiking neurons from the hippocampus or the primary somatosensory cortex. K-nearest neighbors shows the most accurate classification of these groups, using action potential width, amplitude, and onset potential as features (inputs into the algorithm), with the addition of a measure of rapidity (acceleration near action potential onset) showing major increases in classification accuracy. Of the three methods for measuring rapidity, inverse of the full width at half of the maximum of the second derivative of the membrane potential ($\ddot{V}_m$) ($IFWd^2$), inverse of the half width at half of the maximum of $\ddot{V}_m$ ($IHWd^2$), and the slope of the phase plot ($\dot{V}_m$ vs. V_m) near AP onset (phase slope), including the

phase slope measure of rapidity increased the accuracy to nearly perfect (weighted f1-score $\geq$ 0.9999). In addition, the use of phase slope and action potential width as the only features for classification produces measures of accuracy, weighted f1-scores, of >0.9996. The results show the value of rapidity in action potential dynamics, the distinct difference between rapidity in APs generated by hippocampal neurons relative to cortical neurons, and low standard deviations for rapidity values in cortical neurons (fast- and regular-spiking). These findings have potential implications for understanding the ion channel dynamics in action potential initiation and propagation, which can improve the modeling of action potentials and neuronal circuits.

ACKNOWLEDGEMENTS

The authors would like to acknowledge Erin E. Flater and Saurabh Gupta for contributions to the FPGA HDL code and FPGA system described in Chapter 3. The work in Chapter 3 was supported in part by a grant from the National Center for Veterinary Parasitology.

TABLE OF CONTENTS

1. Introduction

Motivation

The motivation for this work is to develop tools and for understanding the electrical properties of cells using machine learning with large data sets. The first part of this dissertation, Chapters 2 and 3, discusses work on creating an impedance cytometer to gather measurements of the electrical properties of parasite eggs found in fecal samples. This work aimed to gather impedance measurements of parasite eggs at multiple frequencies, simultaneously, in order to create a profile over time for each frequency, providing ample information for supervised machine learning analysis. A proof-of-concept device was created and tested, showing feasibility of acquiring this type of data. This work exposed technical challenges related to fabrication and repeatability of mechanical components. These challenges are discussed and may provide insights for future work.

To meet the objective of using machine learning to better understand electrical properties of cells, the second part of this dissertation discusses work using machine learning methods to classify different types of neurons, grouped based on firing patterns (regular-spiking or fast-spiking) and region of the brain (cortex or hippocampus), based on action potential (AP) profiles The work described shows the value of rapidity (acceleration near AP onset) in AP dynamics, the distinct difference between rapidity in APs generated by hippocampal neurons relative to cortical neurons, and the consistency of rapidity in cortical neurons (fast- and regular-spiking). These findings have potential implications for our understanding of ion channel dynamics in AP

initiation and propagation, which can improve modeling of action potentials and neuronal circuits.

Dissertation Organization

This dissertation consists of six chapters. The first chapter is an introductory chapter establishing the motivation for this research and the organization of the dissertation. The second chapter is background and a literature review on impedance analysis of parasite eggs. The third chapter is a manuscript that was published in the Bioinstrumentation Journal for the 2022 Rocky Mountain Bioengineering Symposium. Chapter 4 is a literature review for the use of rapidity as a feature in AP analysis using machine learning. Chapter 5 discusses the results and conclusions for machine learning analysis of publicly available electrophysiology recordings from fast-spiking and regular-spiking neurons from both the hippocampus and the cortex. Chapter 6 contains the conclusion of this dissertation and suggested future work.

2. Literature review

Background

A parasite is an organism that lives on or in another organism, known as the host, and survives and grows by taking nutrients from the host, typically causing harm. Many diseases in cattle are caused by parasites, including helminths and protozoa. Helminths are a group of multicellular organisms, including, but not limited to members of the platyhelminths (flatworms) and nematodes (roundworms). Protozoa are single-celled organisms and include sarcodonia (amoeba), mastigophora (flagellates, e.g., *Giardia* spp., *Leishmania* spp.), Ciliophora (ciliates), and sporozoa (non-motile adult stage, e.g. *Plasmodium* spp., *Cryptosporidium* spp.) ("CDC - Parasites," 2022). This work will focus on helminths and protozoa, as certain species within these groups can be transmitted through ingestion of eggs, cysts, or oocysts from contaminated food and water or the environment.

Parasitic infection often occurs upon ingestion of the egg, cyst, or oocyst stage, in which case the developing organism is encased in a protective shell, often allowing it to survive in environmental conditions (e.g., in soil or water) for extended time periods before infecting a new host. Infection generally occurs when these eggs, cysts, or oocysts are ingested by the host, after which time the parasite can continue to develop and propagate within the host. In humans, intestinal parasitic infections can sometimes occur by consumption of undercooked meats, by a fecal-oral route, which can occur via contaminated water sources or direct contact with contaminated fecal matter, or other mechanisms.

Efforts to control parasitic infection may involve treatment and testing of water sources and environmental samples, diagnosis, chemotherapeutic control of infections in livestock, alteration of management practices, and improved efforts to better understand the diverse life cycles of various parasites across numerous host species. Many infections can easily be treated using anthelmintic or antiprotozoal drugs, but challenges persist in the proper and early diagnosis of these infections.

Providing parasitologists, producers, and others with improved tools for diagnosing parasitic infections would allow for more frequent testing and targeted treatment. Characterization and identification of parasite eggs in stool samples could provide a valuable tool for veterinary and human diagnostics, as parasitic infections are often diagnosed by examination of fecal samples for the presence of eggs, cysts, and oocysts. Current methods require costly equipment and/or trained technicians, creating barriers to frequent diagnostic testing. This is especially critical in cattle and other livestock operations, where parasite monitoring and control practices can contribute to overall herd health, reduce economic burden, and slow the increase in anthelminthic resistance.

State-of-the-art

Parasite Diagnostics- Fecal Egg Counts

Kato-Katz thick smear. The Kato-Katz technique is commonly used in public health for monitoring soil-transmitted helminths in large-scale treatment programs, but is difficult to standardize (Levecke et al., 2011). This technique involves sieving a fecal sample through a mesh, smearing onto a microscope slide using a mold with a cylindrical hole, placing a cellophane sheet soaked in dye and glycerol solution (glycerol-malachite green or glycerol-

methylene blue) over the sample and sandwiching for at least one hour to allow fecal matter to clear, then identifying and counting eggs/cysts under a microscope.

Fecal Flotation. Fecal flotations utilize a sugar- or salt-based flotation solution with a specific gravity of 1.27 (which can be adjusted for different types of eggs), which allows the eggs/cysts to float to the top while most of the fecal debris sinks. The modified double centrifugation technique is performed by mixing a fecal sample with water, filtering large debris using a tea strainer, centrifuging to condense the sample, and pouring off the supernatant to prepare the sample. The sample is then mixed with the flotation solution and centrifuged with a cover slip on top of the tube. The cover slip is then lifted and placed directly onto a glass slide for analysis under a microscope (Foreyt, 1989).

FLOTAC. The FLOTAC device is a plastic apparatus that can be filled with fecal sample mixed with flotation solution, loaded into a centrifuge, then examined under a microscope (Cringoli et al., 2010; Utzinger et al., 2008). The top part of the apparatus rotates to pull the floating sample from the material underneath to a counting grid where eggs can be quantified under the microscope. Though this simplifies the protocol, it still requires costly laboratory equipment and a trained technician to identify eggs.

Mini-FLOTAC. The mini-FLOTAC is adapted from the FLOTAC method but uses passive flotation to float eggs from samples placed in chambers on the device. This allows the mini-FLOTAC to be used without a centrifuge, but still requires evaluation of images for the identification of eggs.

McMasters method. For the McMasters method, a fecal sample is mixed with a salt-based flotation fluid with precise measurement of each for quantitative analysis (4g fecal sample with

26mL salt solution, depending on the protocol used). The sample is sieved to filter larger debris, then placed directly into the counting chambers of a standard McMasters slide for evaluation using a microscope. Two 150uL compartments marked with grid lines are filled with the fecal suspension and placed under a microscope. The eggs float to the top of the chambers, so the microscope can be focused on the top markings of the chamber to provide visualization of the appropriate plane for counting eggs, which can be converted to egg per gram counts using a simple conversion. The FECPAK method is similar to the McMasters method but uses larger sample volumes (~20g fecal), which can be helpful for detecting lower egg counts.

Fecal Egg Count Reduction Test (FECRT). Fecal egg counts are taken from the same pool of animals before and after drug treatment, to determine efficacy of drug treatment. Depending on the drug being tested, the post-treatment samples are taken between 7 and 21 days after the pre-treatment sample (COMBAR, Combatting Anthelmintic Resistance in Ruminants, 2021). The percentage reduction in fecal egg counts is

$$Percentage\ Reduction = 100 \times (1 - \frac{\bar{x}_T}{\bar{x}_0})$$

where $\bar{x}_T$ is the average egg count after treatment and $\bar{x}_0$ is the average egg count before treatment. Fecal egg counts should be performed using a minimum of 20g of rectal fecal sample per animal, from a minimum of 10 animals per group, using any of the previous egg count methods (COMBAR, Combatting Anthelmintic Resistance in Ruminants, 2021).

Image processing algorithms. Image processing algorithms have been developed for identifying parasite egg types in microscope images of fecal samples. Though this removes the need for highly trained technicians to read the results, many of the current systems require a

microscope for imaging, pre-labeling to increase contrast for smartphone interfacing, or have low accuracy (compared to mini-FLOTAC) (Scare et al., 2017).

Single-cell quantification & characterization

Current methods for gathering data about the electrical properties of individual cells include patch clamping, dielectrophoresis, and electrorotation. Patch clamping involves suctioning the cell membrane into the end of a micropipette tip, which creates a resistive seal and allows for quantification of membrane capacitance(Chen et al., 2015). This method is effective but invasive and not suitable for high-throughput data acquisition. Dielectrophoresis uses an applied electric field to polarize particles in suspension and gather information on dielectrophoretic force on the particles, which can be used to calculate dielectric properties(Sun and Morgan, 2010). This method is effective in gathering electrical properties by averaging over a population of cells/particles and is limited in its efficiency for single-cell property characterization. Electrorotation also uses an applied electric field to induce a dipole on the particle. In this method, the electric field is rotating, which exerts torque on this induced dipole and rotates the particle(Sun and Morgan, 2010). The angular velocity (as a function of frequency) is used to calculate the torque, which can be used to generate magnitude and phase information(Chen et al., 2015; Sun and Morgan, 2010). These techniques are limited when it comes to high-throughput screening. Bioimpedance measurements, which will be discussed in the following section, have been recognized as a promising alternative for non-invasive high-throughput characterization of single-cell electrical properties, and has more recently been applied in flow cytometry.

Flow cytometry is a technology that is used in biological research to count and characterize individual cell properties. Conventional flow cytometry requires pre-labeling molecules with fluorescent markers, which requires the ability to fluorescently label and prior knowledge of the

component(s) of interest. Cells are then passed single file through a detection device, which typically consists of a laser used to excite fluorescent molecules from the pre-labeled cells. Though this can be multiplexed, it has a limit to the number of fluorescent tags, requires a trained technician for pre-processing, operation, and data analysis, and uses costly instrumentation.

More recently, cellular properties have been characterized using impedance readings measured across a channel through which cells pass one-by-one. Single-cell properties can be determined from these impedance readings from different frequencies of applied alternating current (AC) by modeling the cell as an electrical circuit (Figure 2.1) using known cellular properties. This concept is an extension of the Coulter Principle developed in the 1940s, which uses a direct current (DC) or single-frequency AC to size and count particles through impedance measurements.

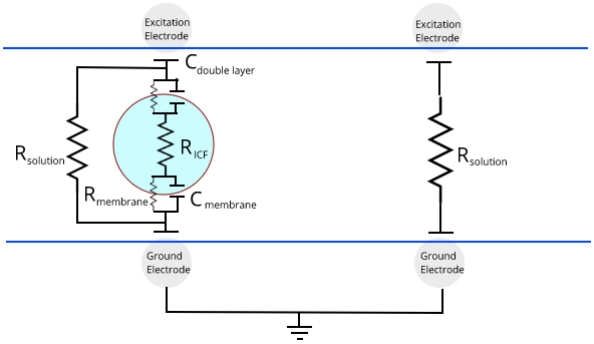

Figure 2.1 *Circuit model of cell in microfluidic channel.* Side view of a microfluidic channel with two sets of parallel electrodes, with the channel walls in blue. The diagram shows the resistance of the solution ($R_{solution}$), cell membrane ($R_{membrane}$), and intracellular fluid (R_{ICF}), and the membrane capacitance ($C_{membrane}$) and double layer capacitance ($C_{double\ layer}$).

The use of multiple frequencies is critical for gathering information about cell characteristics in addition to volume. Table 2.1 shows the range of frequencies used to measure cell characteristics in various MIC devices in the literature (Cheung et al., 2005).

Table 2.1: *Cell Characteristics and Corresponding MIC probing frequencies*

Cell Characteristic	**Frequency**
Electrical double layer*	< 100kHz
Cell size	100kHz-1MHz
Membrane capacitance	2-5 MHz
ICF resistance	10-100 MHz

**This is not a cell characteristic. The electric double layer is formed at the interface between the electrode and the solution from ions gathering on the surface due to chemical reactions, followed by another layer of oppositely-charged ions being draw over those in a diffuse layer, creating a charge double layer, which acts a capacitor and causes phase change in the AC signal.*

This concept, often called microfluidic impedance cytometry (MIC) or electrical impedance (or dielectric) spectroscopy, is being explored for investigating mammalian and bacterial cells, but has yet to be thoroughly explored for examining parasite egg counts or other properties, particularly from fecal samples, which are used for the diagnosis of many types of parasitic infections. A recent publication shows impedance measurements for *Giardia* and *Cryptosporidium* (oo)cysts (McGrath et al., 2017), which have thick outer shells, but are commonly spread through and can be sampled in water and are much smaller than many other common egg types. The differences in size, shape, and composition of the structural features of parasite eggs, including thick outer shells and diversity of inner compartments, relative to bacterial and mammalian cells implies that these measurement frequencies would need to be adjusted to detect these features. The proposed work explores the detection of parasite eggs from complex fecal samples using microfluidic impedance cytometry and aims to optimize frequency and other system parameters to better understand the utility of MIC for determining fecal egg counts in parasitology.

3. Multifrequency microfluidic impedance cytometer using a field-programmable gate array for parasite egg analysis[1]

Overview

Microfluidic impedance cytometry (MIC) has been shown to be effective in the counting and classification of mammalian and bacterial cells but has not been thoroughly explored for the identification of parasite eggs in fecal samples. This study provides preliminary evidence for investigating multifrequency MIC for detecting and counting parasite eggs in such complex samples based on impedance profiles at two frequencies: 500kHz and 10MHz. These frequencies are simultaneously applied to a microfluidic channel and the current through the channel is measured using a field-programmable gate array (FPGA) functioning as two lock-in amplifiers to separate the measurements by frequency. Data from multiple frequencies will allow for the extraction of properties relating to the egg's structural composition, in addition to size. The magnitude and phase measurements for each frequency are sampled at 1kSa/s to provide an impedance profile over time as an egg flows past the electrodes. Impedance profiles from 70μm diameter glass beads, comparable in size to strongyle-type parasite eggs, have been acquired. These proof-of-concept results support the exploration of MIC using an FPGA for performing parasite egg counts, which would open the door for the development of field-deployable parasite diagnostic testing in place of visual analysis of samples in centralized labs.

---

[1] J.E. Nejad, A.C. Mugdha, J.W. Wilson, A.K. McGrew, and K.L. Lear, "Multifrequency Microfluidic Impedance Cytometer Using a Field-Programmable Gate Array for Parasite Egg Analysis", Proceedings of the *Rocky Mountain Bioengineering Symposium* (also published in *Biomedical Sciences Instrumentation*), vol. 56, pp. 184-191, April 2020.

Introduction

Parasitic infection in cattle is often associated with decreased growth and productivity(Clark et al., 2014). Regular deworming is a common practice among cattle producers to mitigate economic loss associated with parasites(Conde et al., 2019). The widespread and frequent use of anthelminthic interventions ("deworming") increases anthelminthic resistance, which is a growing concern among producers and veterinarians (Baiak et al., 2018; Gasbarre, 2014; Sutherland and Leathwick, 2011). More frequent diagnostic testing for monitoring of herds would allow for targeted treatment of cattle with high fecal egg counts. The efficacy of anthelminthic treatment is assessed via fecal egg count reduction tests (FECRT), which compare the fecal egg counts before, and 10-14 days after, treatment(Gasbarre, 2014). Egg counts are determined via isolation of parasite eggs from fecal samples using a fecal flotation technique, followed by visual inspection under a microscope for enumeration and categorization of eggs. The need for costly microscopy equipment and trained technicians typically requires cattle producers to send fecal samples to a central testing facility, which contributes to costs and turnaround times. Additionally, some current practices in parasite control programs may contribute to the development of anthelmintic resistance, over time; improved diagnostics could allow producers to develop more sustainable approaches or implement targeted deworming programs. A low-cost, compact, and easy-to-use diagnostic tool for counting and categorizing parasite eggs would greatly increase economic feasibility for cattle farmers to utilize fecal egg counts for both targeted treatment and testing via FECRT.

Microfluidic devices provide a compact platform with the potential to integrate computerized data analysis for portable automated diagnostics. Microfluidic impedance cytometry (MIC) has demonstrated efficacy as a label-free method for the enumeration and classification of

certain types of mammalian, bacterial, and yeast cells(Chen et al., 2015; Clausen et al., 2018; Sun and Morgan, 2010). The utility of MIC has not yet been explored for performing fecal egg counts, but could provide a promising alternative to central lab testing.

MIC is based on the Coulter principle. When an electrolytic solution is placed in a gap between two electrodes and a current is applied, the measured impedance between the electrodes is dependent on the conductivity of the solution. In the late 1940s, Wallace Coulter showed that when a particle suspended in an electrolytic solution passes through this gap, the change in impedance is proportional to the volume of the particle(Graham, 2003).The temporary impedance change manifests as a pulse in the voltage or current measurement, where the integrated area of the pulse indicates the volume of the particle. This concept is utilized in Coulter counters, where direct current (DC) or low-frequency alternating current (AC) is used to count and size cells and particles for research and medical applications.

The use of multiple frequencies for AC impedance measurements of biological cells can provide information about certain aspects of the cell based on the polarization of its structural components. To separate the electrical properties of these components, cells must be probed at appropriate frequencies for the size, composition, and structure of the feature being investigated. Probing at multiple frequencies simultaneously reveals information about multiple aspects of the same cell, including size, membrane capacitance, and intracellular fluid resistance(Cheung et al., 2005). The combination of this frequency information with impedance measured over time as the cell passes the sensing region provides a "profile" for each cell (Gawad et al., 2004). Based on this concept, multifrequency MICs have been shown to be effective in counting and categorizing certain types of mammalian, bacterial, and fungal (yeast) cells based on their electrical properties(Chen et al., 2015; Clausen et al., 2018; Sun and Morgan, 2010). More recently, MIC

has been used for counting and distinguishing between *Giardia* and *Cryptosporidium* (oo)cysts/eggs in water samples, demonstrating the utility of impedance measurements of parasite (oo)cysts/eggs ranging from 4-14μm (McGrath et al., 2017). Though these specific types of parasites spread through water, many parasite infections, including those in cattle operations, spread by the ingestion of fecal matter from an infected intermediate host. Additionally, many parasitic nematode eggs in cattle, such as strongyle-type eggs, are on the scale of 35-100μm. This work explores initial feasibility for the use of MIC for the enumeration of strongyle eggs through microfabrication of a MIC device capable of analyzing particles in this size range. This paper demonstrates proof-of-concept for the use of multifrequency MIC for performing fecal egg counts. Measurements from glass beads of comparable size to commonly found parasitic nematodes of cattle are presented. Device fabrication, electronics, data processing, and experimental results are discussed.

Methods

Electrode Fabrication: Lift-off Processing

Planar electrodes were patterned onto glass microscope slides with chromium and gold in a standard lift-off process. Glass slides were cleaned and coated with a ~5μm layer of Shipley's S1813 positive photoresist using a Laurell spin coater (3500rpm, 30s), followed by baking on a hot plate for 1 minute at 135°C to harden. The slides were then patterned by UV light exposure using a Microtech LW405C laser writer to pattern the custom electrode design. The design was created in AutoCAD and formatted to Caltech intermediate format (.cif) using CleWin software. Exposed slides were then developed in Microposit MF-319 developer to wash away photoresist in patterned regions, exposing glass. A 50nm layer of chromium, for adhesion to glass, and a 200nm

layer of gold were thermally evaporated onto the surface of the slide. Slides were then soaked and washed in acetone, removing the photoresist and leaving the Cr-Au electrode pattern.

Channel Fabrication and Assembly

Inlet and outlet through-holes were drilled through an electrode-patterned slide using a diamond-coated drill bit. Flexible polymer (Tygon®) tubing was then aligned with the 1.5mm diameter holes and adhered directly to the side of the glass slide without electrodes. A sheet of 3M 468 adhesive transfer tape (130µm thickness) was laser cut to create 100µm-200µm wide channels, as shown in Figure 3.1. Channels were aligned with the through holes and adhered perpendicular to the electrodes on one slide, then aligned and adhered to the opposite slide (electrodes facing the channel) with a widthwise offset to allow connection to electrode leads. Headers were then attached to the leads using silver paint for electrical continuity followed by liquid electrical tape for adhesion. The final fabricated MIC device is shown in Figure 3.1a.

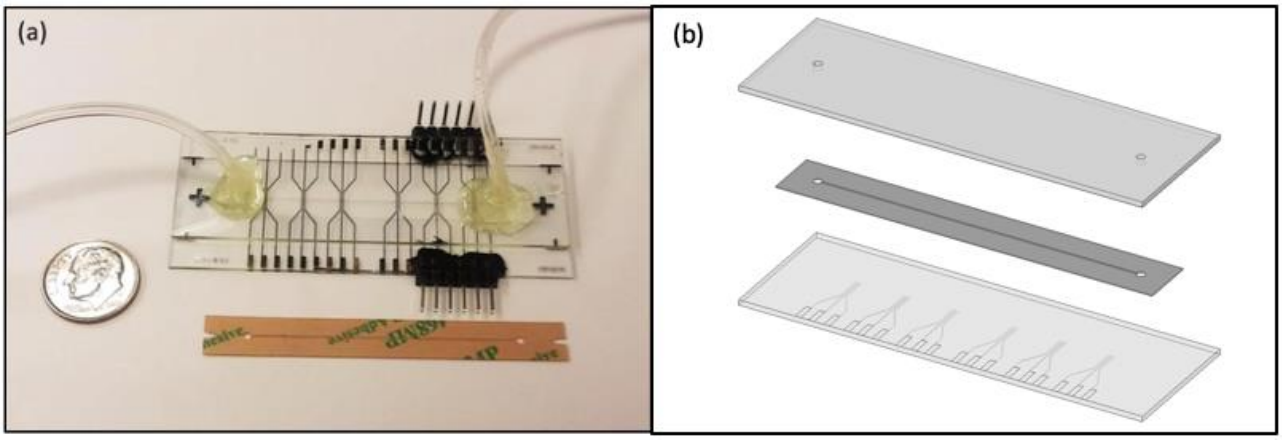

Figure 3.2 *(a) Microfluidic Impedance Cytometer device (top) and laser-cut adhesive channel (bottom) and (b) Layers of MIC device.* (a) The assembled MIC device with inlet and outlet tubing adhered with epoxy, electrode-patterned slides (one facing up and one facing down) forming the top and bottom of the channel, transparent laser-cut adhesive transfer tape between to form sidewalls of channel, and electrical headers for FPGA connection. Below the device is a double-sided adhesive sheet (with paper backing) that has been laser cut to form a ~200µm wide opening

that is placed between the two electrode slides and creates the side walls of the microfluidic channel. Note: this is the current electrode pattern (b) CAD layout illustrating stacked assembly of down-facing electrode slide with drilled inlet and outlet holes (top), adhesive channel (middle), and up-facing electrode slide (bottom).

Field-Programmable Gate Array

As shown in Figure 3.2, an Altera DE2-115 field-programmable gate array (FPGA) was used to apply a multifrequency (500kHz + 10MHz) sinusoidal voltage through a digital-to-analog converter (DAC) output channel and measure the current (using an internal current-viewing resistor) through two analog-to-digital converter (ADC) input channels. The DAC output was connected to the two top electrodes of the MIC device; the ADC channels were each connected to one of the two bottom electrodes, which have an edge-to-edge separation of 180 μm; and the ground connections for all three were connected to each other. The FPGA was programmed in VHDL, modified for use in this application from previous work (Wilson et al., 2015) to function as a multi-channel lock-in amplifier, filtering each of the ADC channel signals to separate the 500kHz and 10MHz contributions using the individual frequencies as internal references to determine in-phase and quadrature components.

The multifrequency AC signal applied through the DAC and read through the ADC channels is sampled at 50MSa/s and decimated (down-sampled) to 1kSa/s using a cascaded integrator-comb (CIC) filter to reduce processing time while maintaining a high enough sampling rate to maintain temporal resolution for time profiling.

Data Acquisition

Data was acquired using Quartus Signal Tap Logic Analyzer software and interfaced with a custom MATLAB script for processing, visualization and storage. In-phase and quadrature

components of the signal from each ADC channel at each frequency were recorded and used to calculate magnitude and phase changes, which were plotted in a series of figures updated in 4-second increments during data acquisition.

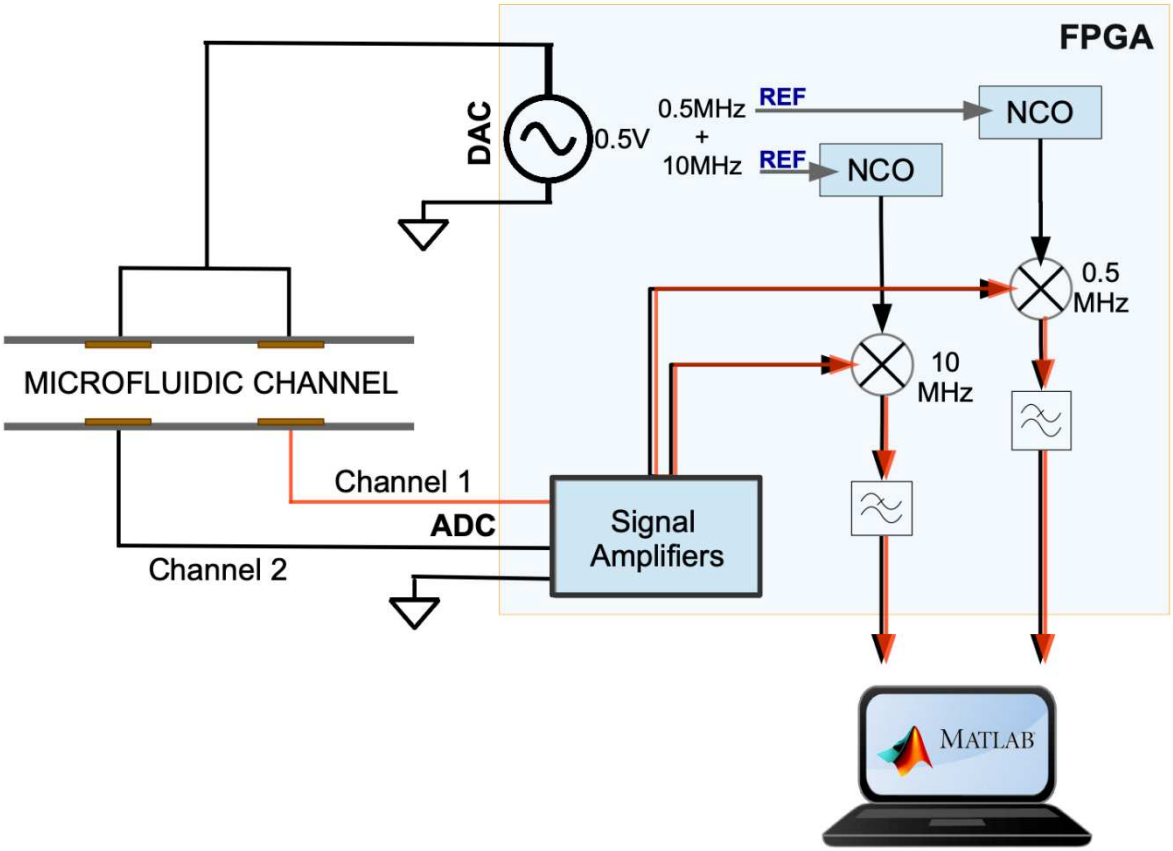

Figure 3.3 *MIC system with FPGA and MATLAB Data Acquisition.* The electrodes on the top of the MIC device channel (left) are connected to the FPGA board (light blue) DAC output and the bottom electrodes are each connected to one of the two ADC input channels. The numerically-controlled oscillators (NCOs) feed into a signal mixer with the ADC signals, then are low pass filtered and output to the PC for real-time visualization and storage in MATLAB (using Quartus Prime software for data acquisition).

Glass bead experiments

The MIC device was aligned under a microscope, attached to a syringe pump via the inlet tubing, and directed to a collection container via the outlet tubing. Video was recorded through a digital camera (Basler scout) interfaced with a microscope and connected to a PC, providing live display and video recording of the sensing region of the channel (Figure 3.3c) using Pylon Viewer software.

The MIC electrodes were connected via headers to the DAC and ADC channels of the FPGA, as described above. The FPGA was connected to a PC and programmed using Quartus Prime software. Quartus Signal Tap Logic Analyzer and MATLAB were run in parallel for acquisition (Signal Tap), visualization and storage (MATLAB) of data.

Before each experiment, normal (0.9%) saline solution (NS), having a specific gravity of 1.0046, was used to gather baseline measurements for calibration. A 10mL syringe was loaded with NS, which was pumped through the device channel at 25μL/min using a syringe pump. Video recording was used to verify the contents of the channel and FPGA data was gathered for baseline measurements. Solid glass microspheres (Cospheric) ranging from 63-75μm were diluted in NS to a concentration of 50 beads/μl and passed through the device channel in the same manner. Video recordings of beads were correlated with timestamps in the acquired data for validation of signal correlation.

Sample Preparation: Fecal Flotation & Egg Isolation

Ruminant fecal samples obtained from the Colorado State University Veterinary Diagnostic Laboratories (CSU-VDL) were processed using a fecal flotation and egg isolation protocol. Fecal samples were weighed and mixed with Sheather's sugar, a media with a specific gravity of 1.27, which is higher than that of eggs and generally lower than that of fecal debris

constituents. Samples were then placed in a centrifuge, a cover slip placed over the tube, and spun to expedite separation of eggs and fecal debris (Foreyt, 1989). The coverslip was then removed vertically and the material attached to the coverslip was moved to another vial and deionized (DI) water added. The vial was centrifuged, supernatant discarded, then filled again with DI water. This washing process was repeated three times to ensure removal of Sheather's solution. After the final wash, supernatant was removed and the pellet was stored in 50µl of DI water at 4^{o}C. Samples can then be diluted for testing in the MIC device.

Results

The normalized impedance measurements when a glass bead suspended in normal saline solution passes between the electrodes in the microfluidic channel are shown in Figures 3.3a and 3.3b. The data was smoothed using an 80-point moving average filter and normalized for each frequency and channel by dividing by the measured baseline impedance of the normal saline solution.

Electrode set (ES) 1 represents the upstream pair of 100µm wide planar electrodes (on the top and bottom of the channel) and ES 2 represents the second pair, 200µm downstream, as shown in Figure 3.3c. The results show a sharp increase in impedance as a bead passes between a pair of electrodes and a smaller increase as it passes the opposite set of electrodes.

Discussion

MIC measurements from glass beads show a distinct increase in impedance as the bead passes each electrode set, as expected. The measured change in impedance (Figures 3.3a and 3.3b) from ES 1 (red) show a primary peak change in impedance as the bead passes between the first set of electrodes, followed by a secondary peak in impedance as the bead passes ES 2. The measured values from ES 2 (blue) show a similar trend. The secondary peak in ES 1 is skewed to the left,

indicating a greater increase in impedance when the bead is passing ES 2 on the side closer to ES 1. The secondary peak in ES 2 is skewed to the right, indicating an increase as the bead is passing ES 1 on the side closer to ES 2. This provides evidence that the secondary peak is due to disruption of the diagonal current path between the top electrode of each set to the opposing (bottom) electrode of the neighboring set.

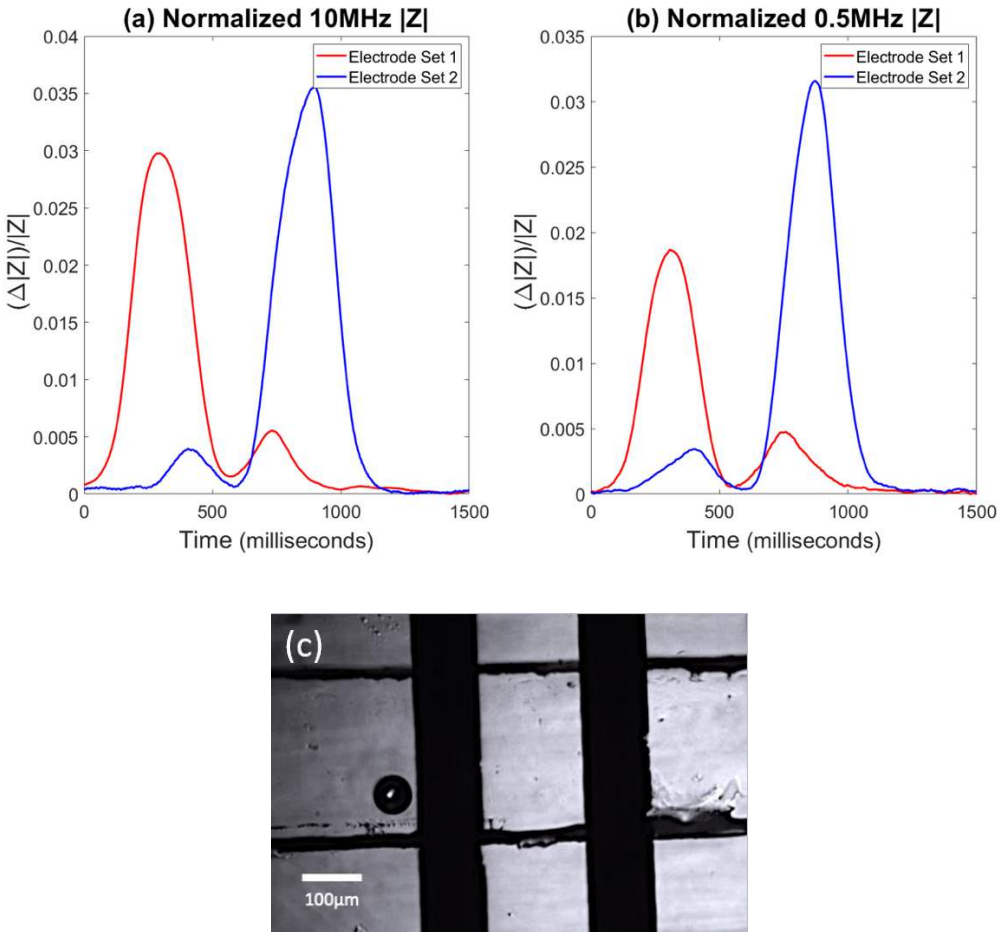

Figure 3.3 *Impedance measurements and image of glass bead in MIC channel.* Time profiles of the change in impedance from the upstream (red, set 1) and downstream (blue, set 2) electrode sets (each set is one electrode on the top slide and one on the bottom slide) recorded simultaneously at (a) 10MHz and (b) 0.5MHz from a 70µm glass bead in normal saline solution as it passes between electrodes in each set. Measurements were sampled at 1000 samples/second and filtered using a moving average of 80 points to reduce noise, then normalized to the baseline FPGA output. (c) Microscope image of a 70µm diameter glass bead suspended in saline solution flowing from left to right in the 250µm-wide MIC device channel between top and bottom electrodes (100µm

wide), passing electrode set 1 (left) followed by electrode set 2 (right), which are separated, edge-to-edge, by approximately 180μm.

The dip between the primary and secondary peaks corresponds to the bead passing an area with a lower density electric field. This is due to the configuration of the 100μm-wide electrodes spaced 300μm apart, center-to-center, on each slide and separated from the electrodes on the opposing slide by a 130μm-thick channel, which creates a longer current path between ES 1 (upstream) and ES 2 (downstream) than between the electrodes in the set (directly across the channel).

The integrated area under the primary peak can be used to determine the size of the bead. The time delay between the peaks measured from each electrode set corresponds to the time it takes the bead to travel through the channel from ES 1 to ES 2. The 600ms delay between the peaks of the traces for the two sets presented in Figure 3.3 corresponds to a velocity of 0.33 mm/s. This is slightly faster than the estimated average fluid velocity of 0.27 mm/s possibly due to the bead traveling near the center of the channel close to the peak of the parabolic fluid velocity profile. Individual particle velocities can be used to compensate for speed when calculating the relative size from integrated pulse area. This information greatly improves the accuracy of the results because even though the volumetric flow rate set by the syringe pump is reliable for measuring the volume pumped out of the syringe, inconsistencies in pressure due to the architecture of the device, minor deformities in channel walls, or momentary partial obstruction of flow can all lead to ephemeral fluctuations in the local flow rate.

The ability to detect ~70μm beads using this MIC device provides a proof-of-concept for the use of MIC to detect similarly-sized parasite eggs. Due to the structural features of many parasite eggs, it is likely that the impedance profiles will be significantly different from other debris that may be in the sample. Fecal flotations can be performed by cattle producers on-site (with a

centrifuge using a Double Modified Centrifugal Flotation (Foreyt, 1989) or alternative protocol (Cringoli et al., 2010)) yielding samples that could be used in a MIC device, with an additional filtration step to prevent clogging of the device channel. This would provide a cost-effective means for producers to more closely monitor the parasite loads on their pastures through frequent sampling and testing, which may greatly reduce the economic burden of parasites in the cattle industry and/or other areas.

Future work will aim to utilize the MIC device for strongyle egg measurements and optimize frequencies and data processing algorithms for accurate classification of parasitic egg types.

Conclusion

MIC has proven to be a valuable tool for the identification and enumeration of various types of cells, but there are still gaps in knowledge in the use of MIC for larger (50-100μm) structures. Better understanding MIC for the analysis of larger samples, such as various types of parasite eggs, would open doors for the use of MIC in a greater breadth of diagnostic applications. This work demonstrated the potential applicability of using an FPGA to function as lock-in amplifiers to improve sensitivity and simultaneously make multifrequency measurements from the same electrode set on a MIC device. Glass microspheres of ~70μm diameter suspended in saline solution were used to verify the function of the electronics. Measurements from 2 sets of electrodes allowed for the determination of the velocity of individual beads, as well as provided previously unpredicted cross-set impedance measurements across the diagonal plane between each top electrode and its neighboring bottom electrode. Applications for this work in the near future includes using multifrequency MIC of parasite eggs to examine internal structure and other characteristics for classification of different egg types.

Disclosures

The authors declare no financial or other conflicts of interest.

Postface: Optimization of Egg Isolation with Debris Analysis

Further experiments were performed in order to optimize the egg isolation protocol used for fecal sample preparation for the purpose of minimizing the amount and size of debris in the samples used for MIC analysis, reducing the probability of clogging the device with debris from the sample. Figure 3.4, below, shows strongyle eggs in a 180 µm-wide microfluidic channel passing a set of 100 µm-wide electrodes. The width of this channel is twice the width of the desired channel width of 100 µm, as it was used to determine if egg samples could pass through the channel height of about 130µm. It can be noted from this image that a 100 µm-wide channel would provide significantly less space for eggs to pass through, and excess debris would cause the channel to clog.

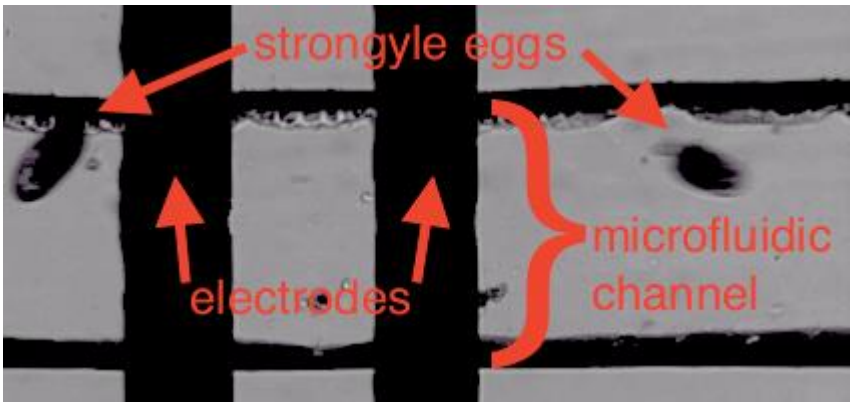

Figure 3.4 *Microscope image of strongyle eggs in a microfluidic channel device.* The channel is made of laser-cut double-sided adhesive with a width of ~180 µm and height of ~130 µm. Electrodes have a width of 100 µm. Strongyle eggs are suspended in NS and samples were prepared using the Gold Standard method.

To determine the optimal protocol to minimize channel clogging, three egg isolation protocols were compared. This was a collaborative effort with Jacey R. Cerda, Emily McDermott, and Ashley K. McGrew. The egg isolation work was performed by Jacey R. Cerda and Emily McDermott, and ImageJ analysis was performed by Jasmine E. Nejad. Three methods for egg isolation were carried out, and the protocols are described below:

Gold Standard

The Parasitology Section at the CSU Veterinary Diagnostic Laboratories (CSU-VDL) currently uses a Standard Operating Procedure for isolating strongyle eggs for the purpose of subsequent molecular identification. It is considered the "gold standard" for the lab, and the one to which we compared the other methods derived and optimized from other published protocols. With some modifications, we performed this method in the following manner: (1) weigh 1 g of sample in a weigh boat, add ~10 ml of DI water and mix thoroughly using a tongue depressor; (2) place 2 layers of cheesecloth in an appropriately sized plastic cup, pour the fecal sample through the cheesecloth, and rinse the weigh dish with DI water. (3) group corners of cheesecloth together and use the tongue depressor to squeeze fecal material vial, rinse the weigh dish with DI water and pour into tube, fill the tube to ~14-15 ml; (5) centrifuge tube for 10 minutes at 360g; (6) remove the tubes and decant, fill tubes half way full with Sheather's solution (SpG 1.27) until an inverse meniscus forms, place a cover slip on top and centrifuge at 360 g for 10 minutes; (7) when centrifuge stops, remove coverslips and carefully tip over a clean 15 ml vial using DI water to gently rinse the coverslips, bring final volume to ~10 ml with DI water, and centrifuge for 10 minutes at 360g; (8) when centrifuge stops, use transfer pipette to remove the supernatant, without disturbing the pellet, leaving 1 ml remaining in the tube, then bring final volume back to ~10ml and centrifuge for 10 minutes at 360 g; (9) once stopped, use the same transfer pipette to remove

the supernatant as in step 8, then resuspend pellet in 1 ml of water; (10) pipette two 50 µl aliquots onto a microscope slide, count all strongyle eggs in each aliquot, sum them, then divide by the number of aliquots for the average number of eggs/50 µl; (11) to determine eggs per gram; then, multiply by 20 which provides the total number of eggs within the 1ml and therefore, 1 g of sample.

Sieve Method

We based this method on Paras et al. (2018) isolation protocol with the following modifications: (1) mix 1 g of fecal material with 25 ml of water; (2) filter slurry through a 355 µm sieve and then through the fluke finder; (3) rinse bottom of fluke finder into a new beaker; (4) poor slurry into vacuum filtration to separate eggs from water; (5) rinse eggs from filter into 15 ml tube with DI water; (6) centrifuge at 360 g for 10 min; (7) aspirate water from pellet leaving ~1 mL egg slurry in the bottom of tube; (8) add 5 mls of Sheather's sugar and mix; then, add Sheather's sugar until inverse meniscus forms, place coverslip on tube and centrifuge for 10 minutes at 360 g; (9) rinse coverslip into tube, add 5-8 mls of DI water and centrifuge for 10 minutes at 360 g; (10) pipette supernatant off until 1 ml remains above pellet; (11) follow procedure as outlined in steps 10 and 11 of Gold Method above.

Salt Method

We based this method on the Mes et al. (2007) isolation protocol with the following modifications: (1) measure out 1 g of fecal sample into weigh boat and mix with 25 ml of MgSO4 solutions (1.3 SpG), homogenize with tongue depressor; (2) pour into 50 ml Falcon centrifuge tube and vigorously shake for 1 minute; (3) poor through metal strainer, rinse 50 mL Falcon tube with tap water and pour filtrate from strainer back into sample tube; (4) centrifuge for 10 minutes at 360 g; (5) transfer supernatant to new 50 ml Falcon tube and add equal amount of DI water, rock tube back and forth to mix; (6) centrifuge for 10 minutes at 360 g; (7) discard supernatant using

pipette, and add 5 ml Sheather's sugar media to pellet, mix well; (8) centrifuge for 10 minutes at 360 g; (9) pipette supernatant into 15 ml tube and at least an equal volume of DI water; (10) centrifuge for 10 minutes at 360g; (11) pipette supernatant off leaving 1ml of water above pellet (if pellet is still not well-formed, discard supernatant as described, add 5 ml DI water to further dilute sugar solution and centrifuge for additional 10 minutes at 360 g); (12) follow procedure as outlined in steps 10 and 11 of Gold Method above.

ImageJ Quantification of Microscopic Debris

For each of 30 samples, three methods were compared: Salt, Sieve, and Gold [Standard]. Ninety slides were prepared by pipetting 50 microliters of isolated eggs onto a slide and then covering with a 22 x 22 mm coverslip. Nine standard images were captured per slide, by dividing the coverslip into a 9-square grid, for a total of 810 total digital images. No eggs were present on these images as only a comparison of debris was made.

ImageJ software (Schindelin et al., 2012) was used to process images and to determine the amount of debris present (size distribution and percent coverage (of coverslip) for each sample. A custom macro (code) was created in ImageJ to automate processing. For each slide, all nine files per sample were combined into one "stack" for sequential processing, combining results from all nine images. For each image in the stack, the "subtract background" tool was used with a rolling 20-pixel filter. The "Find Edges" tool was then used to find the edges of objects in the image by determining borders with the highest contrast. It was then converted into an 8-bit image, meaning each pixel had 256 possible values, ranging from 0 to 255. The 8-bit image was thresholded with a dark background, removing all values below 43. The "de-speckle" tool was then used to remove background pixels, and the "Analyze Particles" tool was then used to produce results including information about the particles in each image over 100 pixels in size, to remove background.

Results were saved for each stack (slide) for each method, processing a total of 810 images from 90 slides. Tables 3.1-3.3 show ImageJ analysis results for each of the three egg isolation protocols.

Table 3.1 shows the percent debris coverage for each of the methods. It can be noted that the standard deviation for each of the methods is greater than the mean, indicating that there is a large distribution of values for each of these methods. The 95% confidence intervals, as well as the minimum and maximum values can be used to compare the different groups. It is clear from the higher confidence interval maximum and maximum values, the salt method produced slides with the greatest percentage of debris coverage, but there is also a very broad distribution of these values. It can be noted that the sieve method shows the least percent coverage, with the gold standard falling between the two others.

Table 3.1: Analysis of Percent Debris Coverage

Method	N	Mean	Std Dev	Std Error	95% Confidence limits of mean		Median	Min	Max
Gold Standard	**30**	15.22	18.74	3.42	8.22	22.22	7.59	0.42	76.46
Sieve	**30**	8.25	8.37	1.53	5.12	11.38	5.05	0.86	27.13
Salt	**30**	17.11	25.31	4.62	7.66	26.56	7.30	0.01	106.07

Table 3.2: Analysis of Average Particle Size (pixels)

Method	N	Mean	Std Dev	Std Error	95% Confidence limits of mean		Median	Min	Max
Gold Standard	**30**	796.93	466.56	85.18	622.71	971.15	698.10	268.61	2134.85

Sieve	**30**	1340.58	1016.21	185.53	961.12	1720.04	1098.65	264.26	4901.21
Salt	**30**	548.43	281.99	51.48	443.13	653.73	428.65	161.50	1172.98

Table 3.3: Analysis of Number of Particles									
Method	**N**	**Mean**	**Std Dev**	**Std Error**	**95% Confidence limits of mean**		**Median**	**Min**	**Max**
Gold Standard	**30**	963.067	1016.91	185.661	583.348	1342.79	560	70	3709
Sieve	**30**	392	602.792	110.054	166.914	617.086	193.5	23	2483
Salt	**30**	1401.73	2123.13	387.629	608.944	2194.52	498	2	8873

Table 3.2 shows the average particle size for each method. It can be observed that the salt method produces significantly smaller particle sizes when compared to the sieve and Gold standard methods. Cased on the maximum particle size, the mean, and the median values, this method produces the smallest particles.

Table 3.3 shows the number of particles in each slide, which can be utilized to better interpret the results when considered along with the particle size and percent coverage. The sieve method had the lowest percent debris coverage and number of particles, but it also had the largest particle size. The salt method has the highest debris coverage, with a larger number of smaller particles. For use with the MIC device, larger particles are more likely to clog the channel, so even though the sieve method had a lower percent debris coverage, the smaller particle size is a more important factor for determining the optimal method for use with the MIC device, so the salt method would be recommended for future work. Additionally, these solutions can be diluted before loading into the device, so the percent debris can be further reduced, but

the particle size cannot be readily changed. It is therefore recommended that the salt method be used for further testing, due to the maximum and average size of particles.

4. Action Potential Dynamics in Neurons - Literature Review

Machine learning methods have been used for the classification of action potentials (APs) for improved understanding of ion channel dynamics of neuron subtypes, modeling of neuronal circuits, and discrimination of neuron subtypes from patch-clamp recordings (Buccino et al., 2018; Ghaderi et al., 2018; Gouwens et al., 2019; Wang et al., 2022).

Ghaderi et al., 2019

A study by Ghaderi et al. evaluates *in vivo* whole-cell patch clamp recordings of APs from excitatory pyramidal cells and two types of inhibitory neurons in the mouse primary visual cortex using a discrete cosine transform to determine discriminatory features, followed by fuzzy c-mean clustering to determine cluster centers, then performing classification using a minimum distance classifier. The discrete cosine transform is used to transform the recordings from the time domain into the frequency domain, from which 100 coefficients are extracted as features for each spike. These coefficients were reduced to two principal components (90% cumulative percentage variance) using principal component analysis. The data was then split into 10 sets, where 9 sets were used for training and one for validation, repeated for a total of 10, for 10-fold cross validation. Fuzzy c-means clustering was used to determine clusters of data with representative centers. The test data was then classified into these clusters using the cluster centers in the minimum distance

classifier (Euclidean distance). This classification had an accuracy of 92.67 $\pm$ 0.54%, precision of 87.13 $\pm$ 2.59%, and recall of 87.05 $\pm$ 0.74%.

In addition, 7 electrophysiological features are extracted from the waveform: AP threshold, AP duration, after hyperpolarization, rise time, fall time, rise rate, and fall rate. These features were evaluated in the same way as the discrete cosine transform. Two principal components were extracted from this feature set (90% cumulative percentage variance) and evaluated using c-means clustering and 10-fold cross validation. This method showed an overall accuracy of 82.29 $\pm$ 1.31%.

To assess performance on *in vitro* APs, data was extracted from 50 neurons from the Allen Cell Types Database from five neuronal subtypes: pyramidal, GABAergic parvalbumin positive, somatostatin positive, 5HT3a, and vasoactive intestinal peptide cells. Classification of these cells using one principal component and 5-fold cross validation yielded an overall accuracy of 84.13 $\pm$ 0.81%. These results show some efficacy in identification of these neuron subtypes, but there is much room for improvement before relying on these methods for classification.

Wang et al., 2022

Wang et al. use a convolutional neural network for the classification of neurons according to their genetic label or general type (excitatory or inhibitory) (Wang et al., 2022). Their work aims to be able to discriminate neuronal types based on electrophysiological recordings alone for the interpretation of experimental data. This study points out the lack of established features for the separation of neuron types and the continuous nature of these spike recordings, lacking clear definition for each AP. The method used in this study is a convolutional neural network with 3 subnetworks. The raw time series data is fed into the first subnetwork, which extracts the real and imaginary components of the Fourier coefficients (fast Fourier transform) and feeds them into the second and third subnetworks.

The researchers attempted to classify five neuronal subtypes, resulting in a test set accuracy of 88.76% for discrimination of 5 genetic neuron types (excitatory, parvalbumin, somatostatin, neuron-derived neurotrophic factor, and vasoactive intestinal peptide cells), with 98.28% accuracy of more general classification between excitatory neurons and inhibitory. Though this shows promise for classification, there is still a need for greater accuracy to be able to use this reliably for the development of neuronal circuits.

These works demonstrate the continuing need for improved classification algorithms for more reliable discrimination of neuron types and more robust models. Accurate modeling will not only improve classification for use in experimental research, but also, can provide insights into the difference in ion channel physiology between different neuronal subtypes.

Sodium Channel Activation

The rapid initiation of APs deviating from the Hodgkin Huxley model (Hodgkin and Huxley, 1952) has been an area of interest for many researchers in the neurosciences, as it has potential implications for our understanding of ion channel dynamics, particularly the physiology of sodium channel activation (Dixon et al., 2022; Huang et al., 2012; Ilin et al., 2013; Naundorf et al., 2006; Telenczuk et al., 2017; Teleńczuk et al., 2015; Venkatesan et al., 2014). These works propose various mechanisms for rapid activation of sodium channels, including cooperative gating, clustering, and back-propagation of the AP into the soma. Sodium channel cooperativity suggests that the activation of a sodium channel will increase the rate of activation of nearby sodium channels, accelerating the depolarization of the membrane. Studies suggest that clustering of sodium channels plays a role in this, with groups of sodium channels activating together (Dixon et al., 2022). It has been found that the alpha subunits of sodium channels dimerize with each other, assembling and gating together as a dimer (Clatot et al., 2017). These

recent findings suggest AP initiation dynamics that differ from the widely accepted Hodgkin Huxley model, leading to questions about how these mechanisms effect neuronal membrane potential during APs, and if these mechanisms are consistent across subtypes.

The following chapter aims to improve classification methods for neuronal APs from multiple subtypes, as well as increase understanding of membrane potential dynamics during AP initiation. Classification results and analysis are presented to show alternative methodology and improvement to classification, as well as insights into potential implications for our understanding of ion channel dynamics, particularly in sodium channel activation.

5. Addition of a rapidity feature in machine learning action potential analysis improves classification of neuron types[2]

Highlights

- The addition of any measure of action potential rapidity, which qualifies acceleration of the action potential near onset, increases ability to discriminate between action potentials generated by regular- and fast-spiking neurons from the hippocampus and the cortex (fast-spiking interneurons and regular-spiking pyramidal neurons from the CA1 region of the hippocampus, and fast-spiking and regular-spiking cortical pyramidal neurons from L2/L3 of the primary somatosensory cortex)
- Addition of the phase slope rapidity measure to the classical action potential attributes (width, amplitude, and onset potential) as features in a k-nearest neighbors classifier produces nearly perfect (f1-score >0.9987) classification of APs generated by cortical and hippocampal regular and fast spiking neurons.
- Phase slope rapidity and action potential width are sufficient to classify nearly all action potentials into regular- or fast-spiking, hippocampal or cortical, where width largely discriminates spiking speed and phase slope discriminates brain region.
- Phase slope rapidity is significantly higher in hippocampal neurons than in cortical neurons, for both regular- and fast-spiking neurons, suggesting distinct differences in the

[2] This chapter contains contents that closely corresponds to a manuscript to be co-authored by Jasmine E. Nejad, Ahmed A. Aldohbeyb, and Kevin L. Lear that will be submitted to a peer-reviewed journal.

physiology of sodium channel activation in neurons in the hippocampus relative to the cortex.

Introduction

Classification of neuron types is a continuously developing area of neuroscience, drawing from advancements in our understanding of the morphology, physiology, and biochemistry of neurons. Understanding differences in action potential (AP) behavior in different neurons provides information for researchers to further subdivide neuron types, creating more accurate and more repeatable models for neuronal circuits. Recent work has shown machine learning models to be an effective tool for neuron classification (Armañanzas and Ascoli, 2015; Ghaderi et al., 2018; Wang et al., 2022). In addition to automated classification of neuron types, developing these models using features that optimize the ability to discriminate between neuron types can provide insight into the electrophysiological differences in neuron types in different brain regions, allowing for more accurate modeling of APs and neuronal circuits, more specific understanding of ion channel behavior during AP initiation and propagation in different types of neurons, and greater understanding of the physiological and cognitive functions of different neurons.

The Hodgkin and Huxley (HH) model of APs assumes sodium ion channels, transporting only sodium ions, and potassium ion channels, transporting only potassium ions, are responsible for the voltage fluctuations observed during an AP (Hodgkin and Huxley, 1952). Though this model has provided a foundational basis for AP modeling, later studies show that there is more complexity to the ion channels present on the cell membranes of different types of neurons (Bean, 2007; Naundorf et al., 2006). Studies have described and measured a “kink” at AP onset, which has also been measured as “rapidity” of AP onset, which qualifies the acceleration of AP onset,

which differs from the HH model, indicating that this feature of APs can be different in neurons from different brain regions (Aldohbeyb et al., 2021; Gutkin and Ermentrout, 2006; Naundorf et al., 2006).

To understand the importance of the rapidity feature in APs in different regions of the brain, a standard method for measurement should be used. This work investigates the utility of three different methods of rapidity measurement in the discrimination of fast-spiking (FS) and regular-spiking (RS) neurons from the hippocampus and the cortex. Using two open-source databases for current-clamp AP recordings, five different supervised machine learning methods, k-nearest neighbors (kNN), decision tree, support vector machine (SVM), logistic regression, and naïve Bayes, were used to discriminate between cortical fast-spiking (cFS) neurons, hippocampal fast-spiking (hFS) neurons, cortical regular-spiking (cRS) neurons, and hippocampal regular-spiking (hRS) neurons. The classically used feature set (classical features) of AP onset potential, AP width, and AP amplitude was used as the baseline set of features for classification. The impact of adding rapidity to these features was analyzed using one of three measures of rapidity: inverse of the full width at half maximum of the second derivative (IFWd2), inverse of half of the width at half maximum of the second derivative (IHWd2), or phase slope measurement, taken as the slope of the phase plot (change in membrane potential vs membrane potential) at a set criterion level (10mV/ms for all measurements in this paper). KNN was found to be the most accurate classifier, based on weighted f1-scores, though classification results from all five classifiers indicate that the addition of any of these measures of rapidity significantly increases the accuracy of classification, and that the addition of the phase slope measure of rapidity results in nearly perfect accuracy (knn weighted f1-score $\geq$ 0.999773). These results indicate that the phase slope measure of rapidity is

an important feature in AP classification and should be considered as a critical component for AP models.

Materials and Methods

Action Potential Recordings

Data Source for Raw Action Potential Recordings

Electrophysiological recordings of APs from adult mice were obtained from two databases. Cortical data from the somatosensory cortex were obtained from the Gigascience database and hippocampal data were obtained from the CRCNS database. Data for cortical neuron recordings, along with detailed experimental protocols for collection of these recordings, can be found in da Silva Lantyer *et al.* (da Silva Lantyer et al., 2018). This data was collected from pyramidal regular-spiking (RS) neurons (n = 27) and fast-spiking (FS) neurons (n = 7) in the L2/3 layers of the primary somatosensory cortex in adult mice. Data from hippocampal CA1 neurons, along with experimental protocols, can be found in Lee *et al*. (Lee et al., 2014). The recordings analyzed from this set are from 17 RS pyramidal neurons and 6 FS interneurons.

AP selection

Each database file contains AP recordings from one neuron, gathered as one continuous recording of membrane potential over time (V_m) in response to a pulsed current stimulus. APs were identified using the criteria previously described (Aldohbeyb et al., 2021). In brief, APs included in this analysis must have come from a current step that contained at least 2 APs and must have an inter-spike interval of at least 30ms for RS neurons and at least 12ms for FS neurons. With these criteria, there were a total of 3733 APs from 6 cFS neurons, 3966 APs from 27 cRS neurons, 888 APs from 6 hFS neurons, and 2637 APs from 17 hRS neurons.

Interpolation

For calculation of rapidity features, an interpolation function was used to interpolate discrete time series data to $\Delta t = 1$ μs. For calculation of IFWd2 and IHWd2, MATLAB's *spline* function was used, which interpolates using a cubic spline function between points. The *spline* function creates dips between points which, for phase slope measurements, drastically increases standard deviation between measurements from spikes in the same spike train. To avoid this issue, MATLAB's *pchip* function was used for phase slope measurements, which uses a cubic Hermite interpolating polynomial in piecewise fashion, preserving shape and respecting monotonicity.

Data Features

Defining Classical Features

The three "classical" features used in AP analysis are width, onset potential, and amplitude. For this analysis, AP onset potential was determined to be the voltage at which the first derivative of the membrane voltage vs. time plot ($\dot{V}_m$) equals 10mV/ms, as defined by Naundorf *et al.*(Naundorf et al., 2006). The AP amplitude was taken as the difference between the onset voltage and the peak voltage. AP width was measured as the full width at half of the AP amplitude.

Defining Rapidity Features

Two of the rapidity measurements were generated using the second derivative of membrane voltage vs. time ($\ddot{V}_m$), as previously described (Aldohbeyb et al., 2021). IHWd2 was calculated as the inverse of half of the width at half of the maximum of $\ddot{V}_m$. IFWd2 was calculated as the inverse of the full width at half of the maximum of $\ddot{V}_m$. The third rapidity measure, phase slope, was measured as the slope of the phase plot ($\dot{V}_m$ vs. V_m) at AP onset (Telenczuk et al., 2017).

Classification Algorithms (Classifiers)

Five different classification algorithms were tested on this data set: kNN, decision tree, SVM, logistic regression, and naïve Bayes. Classification was performed in python using Jupyter Notebook, using the scikit-learn package. All data was standardized using the StandardScaler function from the sci-kit learn package prior to classification. For kNN, KNeighborsClassifier was used with k=3. For SVM, svm.svc (C-support vector) was used as the classifier with the one-versus-one decision function shape. For logistic regression, the maximum number of iterations for convergence was set to 10,000. For all classifiers, 4 feature sets were used. Classical Only contains the classical features of AP onset, AP width, and AP amplitude. The other three sets contain the classical features in addition to one measure of rapidity: Classical + IFWd2, Classical + IHWd2, or Classical + phase slope.

Results & Discussion

F1-scores for classifiers

Weighted F1 scores were used as the metric for evaluating each classification. Weighted scores are calculated by calculating the average f1-scores for each class, then using the number of instances of that class as a weight. F1-scores account for both precision and recall, and are

The weighted f1-scores for each classifier and each feature set are shown in Figure 5.1. F1-scores were computed by taking the average value (number of AP's mislabeled) for each neuron class weighted by support (total number of APs per neuron type), averaged over 50 randomized repeats of stratified 5-fold cross validation. Weighted scoring and the use of stratified sets (each set contains the same proportion of each neuron type) account for the imbalance in the number of APs from each neuron type.

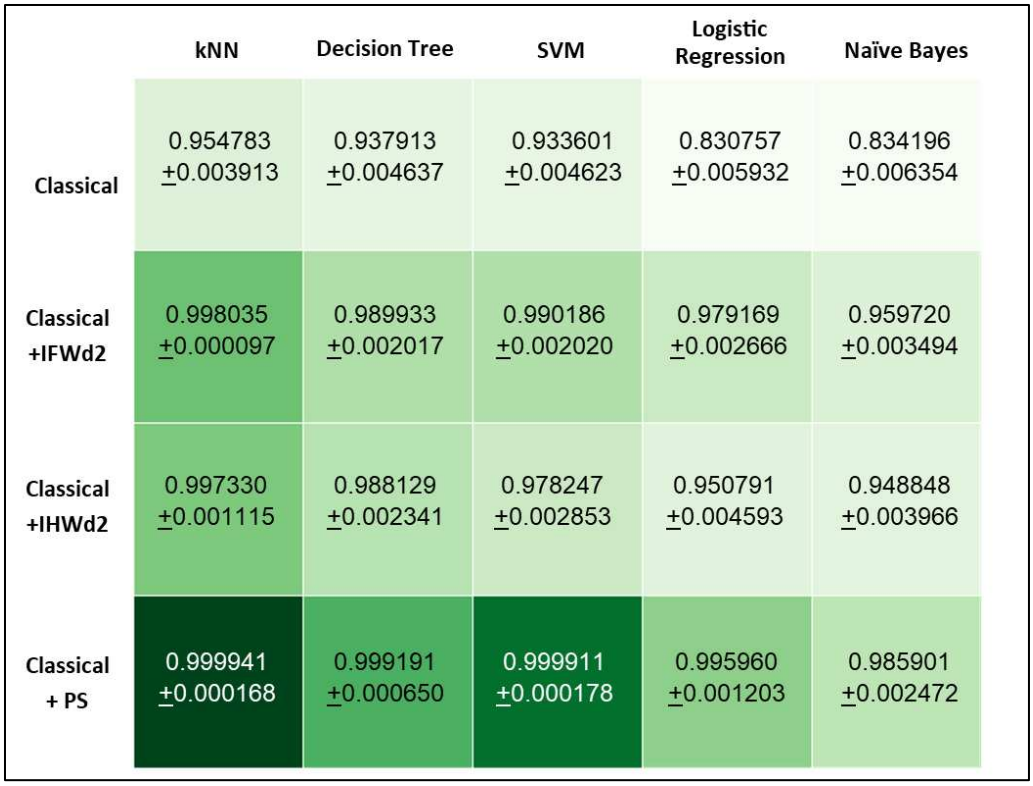

Figure 5.1: *Heatmap of weighted average f1-scores for 50 repeats for each classifier (columns) using each feature set (rows) for stratified 5-fold cross-validation.* Darker cells indicate higher f1-scores. Features: (Classical) classical features of AP width, AP Amplitude, AP onset. (Classical + IFWd2) Classical features plus rapidity feature measured using the inverse of the second derivative taken over the full width at half of the maximum voltage value. (Classical + IHWd2) Classical features plus rapidity feature measured using the inverse of the second derivative taken over half of the width at half of the maximum voltage value. (Classical + PS) Classical features plus phase slope measure for rapidity.

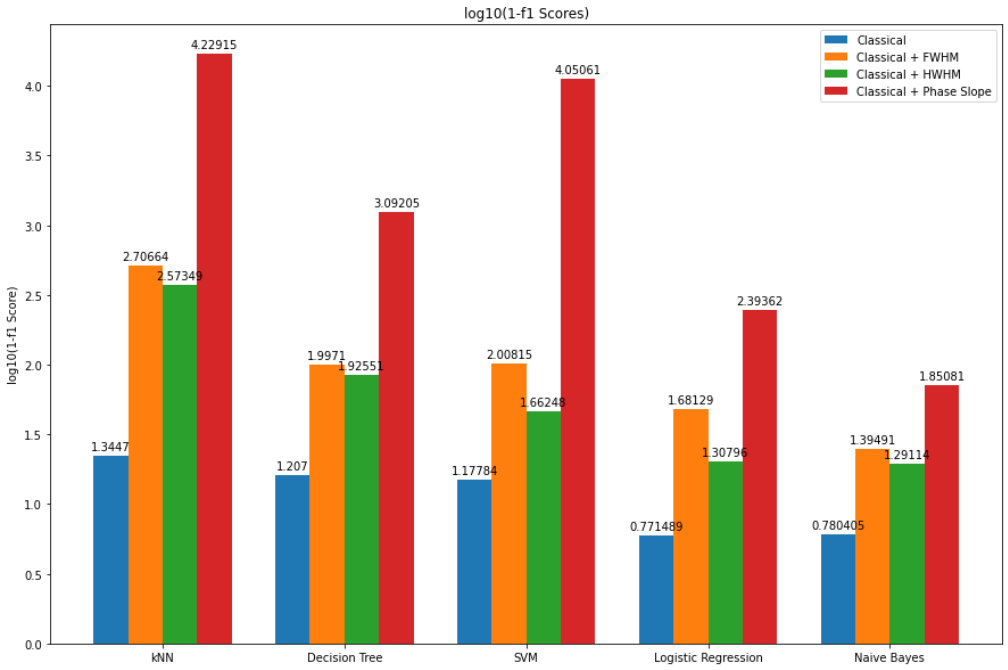

Figure 5.2: ***Log-scale f1-score bar chart***: *log_{10}(1-f1Score) values for each classifier and each feature set*. kNN is k-nearest neighbors classifier (k=3) and SVM is support vector machine classifier. Classical indicates the use of classical features only (AP width, AP amplitude, AP onset potential). FWHM (full width at half maximum), HWHM (half width at half maximum), and Phase Slope indicate the addition of these rapidity measures. Larger values indicate greater f1-scores and greater precision and recall. Values plotted as $|\log_{10}(1\text{-f1Score})|$ to better visualize differences.

The absolute value of the $\log_{10}$(1-f1-score) is shown in Figure 5.2 for visualization of trends across feature sets and classifiers. The same trends can be seen across all five algorithms, showing classical features plus phase slope rapidity to have the highest f1-score for each classifier, followed by IFWd2, IHWd2, then classical features alone as the lowest f1-score for each classifier. These results indicate that the addition of any measure of rapidity to the classical feature set increases classification accuracy. This is expected, as more information is being added to the model, though the addition of features with little or no influence on discrimination of these neuron types (adding little to no information to the model) would lead to overfitting and a lower f1-score. Since all measures of rapidity increased f1-scores across all classifiers, rapidity adds information to the model that is not present in the classical features, as well as information that is useful in

discrimination of the neuron types in this data. Of these rapidity measures, the addition of the phase slope measurement to the classical feature set shows the highest f1-scores. Since the phase slope measure of rapidity shows the greatest improvement in classification performance, this rapidity measure was used for further evaluation. Since the kNN classifier showed the highest f1-scores for all the feature sets, and all the classifiers showed similar trends across feature sets, kNN was used as the classifier for comparison of feature sets in further analysis.

Confusion Matrices

The confusion matrices for the classical features alone, and classical features plus a measure of rapidity (IHWd2, IFWd2, Phase Slope), can be seen in Figure 5.3. The results show that classical features alone always classified cFS neurons correctly, and nearly always classified hFS neurons correctly, indicating that these features are sufficient for the discrimination of fast-spiking neurons. The decreased ability to discriminate regular-spiking neurons (~92%), indicates that the classical features are not as distinctly different between cortical and hippocampal regular-spiking neurons. The results from the addition of any measure of rapidity add significant value to the classification algorithm, increasing the accuracy of classification of regular-spiking neurons to >99%, without reducing ability to discriminate fast-spiking neurons. In particular, phase slope showed the most accurate results of all feature sets, indicating that phase slope measurements provide critical information about regular-spiking neurons that is distinct between neurons in the hippocampus and those in the cortex.

Predicted Class

True Class

Classical Only	cFS	cRS	hFS	hRS
cFS	**1.0 (3733)**	0.0 (0)	0.0 (0)	0.0 (0)
cRS	0.0 (0)	**0.928326 (3681.74)**	0.0 (0)	0.071674 (284.26)
hFS	0.000068 (0.06)	0.0 (0)	**0.999932 (887.94)**	0.0 (0)
hRS	0.000144 (0.38)	0.083921 (221.30)	0.0 (0)	**0.915935 (2415.32)**

Classical + IFWd2	cFS	cRS	hFS	hRS
cFS	**0.999989 (3732.96)**	0.000011 (0.04)	0.0 (0)	0.0 (0)
cRS	0.000121 (0.48)	**0.997257 (3955.12)**	0.0 (0)	0.002622 (10.40)
hFS	0.0 (0)	0.0 (0)	**1.0 (888)**	0.0 (0)
hRS	0.0 (0)	0.004133 (10.90)	0.0 (0)	**0.995867 (2626.10)**

Classical + IHWd2	cFS	cRS	hFS	hRS
cFS	**0.999989 (3732.96)**	0.000011 (0.04)	0.0 (0)	0.0 (0)
cRS	0.000061 (0.24)	**0.996737 (3953.06)**	0.0 (0)	0.003202 (12.70)
hFS	0.0 (0)	0.0 (0)	**1.0 (888)**	0.0 (0)
hRS	0.0 (0)	0.006780 (17.88)	0.0 (0)	**0.993220 (2619.12)**

Classical + Phase Slope	cFS	cRS	hFS	hRS
cFS	**1.0 (3733)**	0.0 (0)	0.0 (0)	0.0 (0)
cRS	0.000166 (0.66)	**0.999834 (3965.34)**	0.0 (0)	0.0 (0)
hFS	0.0 (0)	0.0 (0)	**1.0 (888)**	0.0 (0)
hRS	0.0 (0)	0.0 (0)	0.0 (0)	**1.0 (2637)**

Figure 5.3: ***Confusion matrices of classical features and classical features plus rapidity (IFWd2, IHWd2, or Phase Slope)*** *reporting classification using the k-nearest neighbors classifier (k=3) with 5-fold cross-validation repeated 50 times for classification of APs generated by fast-spiking (FS) or regular-spiking (RS) neurons from the cortex (c) or the hippocampus (h).* True neuron class for each AP is represented by the row, and the class predicted by the classifier is shown by the column, with the yellow cells indicating correct classification (predicted class = true class). Green shows FS and white shows RS. Top values are normalized for each row and bottom values are average total counts (for one repeat) over 50 repeats. Features used in each set: (Top left) Classical features alone (AP amplitude, AP width, AP onset potential). (Top right) Classical features plus rapidity feature measured as the inverse of the full width measured at half of the maximum of the second derivate of voltage vs. time plot (IFWd2). (Bottom left) Classical features plus rapidity feature measured as the inverse of the full width measured at half of the maximum of the second derivate of voltage vs. time plot (IHWd2). (Bottom right) Classical features plus Phase Slope rapidity measure, measured as the slope of the phase plot at a set criterion level.

Figure 5.4 shows confusion matrices for kNN using phase slope only, width only, and width + phase slope as the feature sets. Using width alone, hFS is classified correctly 100% of the time, meaning that AP width is distinctly different in these neurons relative to the other groups. Width alone shows some efficacy in discriminating FS neurons from RS neurons but is less

effective in discriminating between hippocampal and cortical RS neurons. Using only phase slope values, there is confusion between FS and RS neurons within the same brain region, but phase slope shows greater ability to discriminate cortical vs hippocampal neurons. Looking at the top two confusion matrices in Figure 5.4, it can be observed that the two confusion matrices complement each other in that where one shows higher confusion, the other shows greater accuracy. The weighted f1-scores for these feature sets are 0.796338 $\pm$ 0.007408 for width alone and 0.620103 $\pm$ 0.008524 for phase slope alone. The bottom confusion matrix in Figure 5.4 shows normalized values and average counts per repeat using phase slope and AP width values as features, which shows a drastic increase in classification, having a weighted f1-score of 0.999636 $\pm$ 0.000382. This is only slightly lower than the f1-score of 0.999941 $\pm$ 0.000168 for Classical + Phase Slope for kNN, and much higher than 0.954783 $\pm$ 0.003913 for the classical feature set alone, suggesting that phase slope is a far more important feature for classification of these neuron types than AP amplitude or AP onset, and that phase slope has more distinct information in comparison to width. These results suggest that the information contained in phase slope and AP width explains the majority of the differences between APs generated by cortical FS, cortical RS, hippocampal FS, and hippocampal RS neurons.

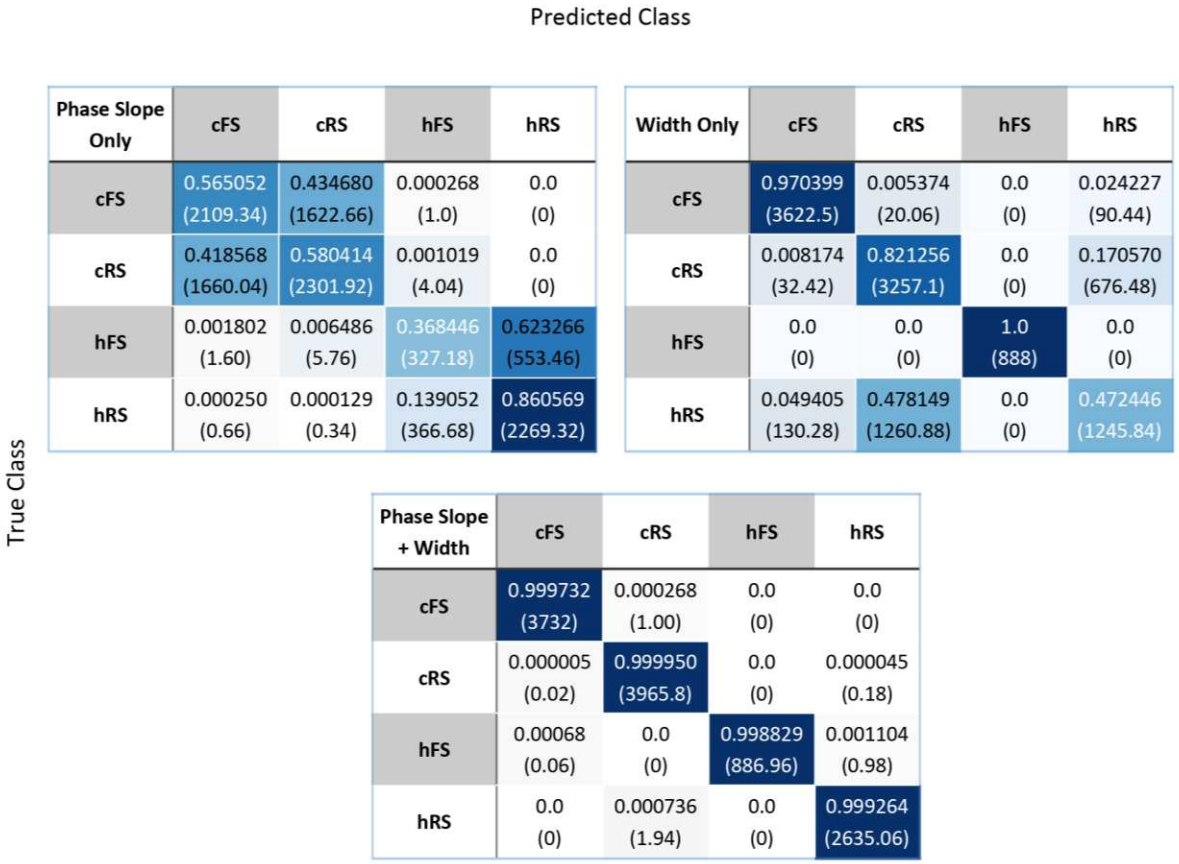

Figure 5.4: ***Confusion matrices heatmap using phase slope only, width only, and phase slope + width as features*** *using the k-nearest neighbors classifier (k=3) with 5-fold cross-validation repeated 50 times for classification of fast-spiking (FS) or regular-spiking (RS) neurons from the cortex (c) or the hippocampus (h).* True neuron class for each AP is represented by the row, and the class predicted by the classifier is shown by the column. Top values are normalized (total per row equals 1.0) and bottom values are average total counts (for one repeat) over 50 repeats. Features used in each set are shown in the top left corner cell. Diagonal cells (top left to bottom right) represent correct classifications. Heatmap shows darker cells for normalized values closer to 1.0.

Depolarization of the membrane that initiates the AP is caused by the activation of voltage-gated sodium channels that open in response to changes in membrane potential. Since rapidity is quantified as the maximum acceleration of the depolarization phase, it can be attributed to the rate of sodium channel activation. This can be thought of as how many new channels are being activated, assuming channels that have already been activated have a constant rate of ion transport relative to the membrane potential. This can also be visualized as a phase plot ($\dot{V}_m$ vs. V_m), where

the phase slope values are derived from. When the peak of the AP is reached, sodium channels begin to deactivate and potassium channels begin to activate, starting repolarization. The width of the AP can generally be attributed to the rate of potassium channel activation during repolarization. Using these interpretations, we can see that using phase slope rapidity and AP width for classification closely parallels classification of neurons by the rate of increase in sodium channel activation, i.e. abruptness, during depolarization and the rate of potassium channel activation during repolarization, respectively (Figure 5.5).

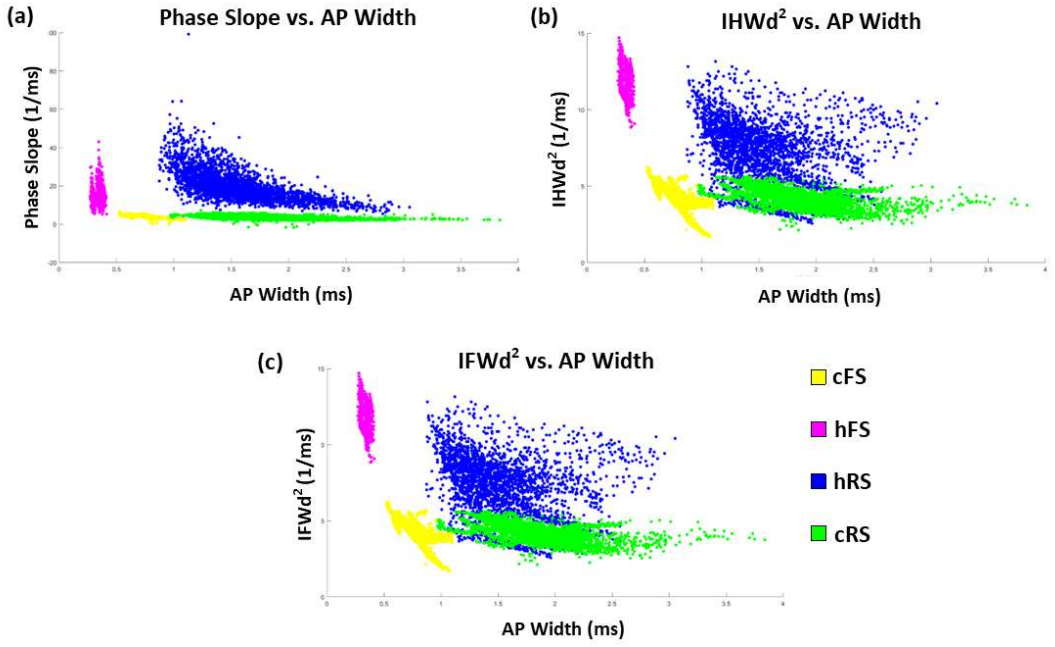

Figure 5.5: Scatter plots of each rapidity feature vs. AP width. Colors show APs from cortical fast-spiking (cFS), hippocampal fast-spiking (hFS), hippocampal regular-spiking (hRS), and cortical regular spiking (cRS).

Figure 5.5 shows a scatter plot of phase slope vs. AP width, where the four different neuron types are shown in different colors. It can be observed that hippocampal neurons show higher phase slope values compared to cortical neurons, for both RS and FS neurons. This suggests that hippocampal neurons, which have higher rapidity, have higher rates of increase in sodium channel activation when compared to cortical neurons. Recent work has hypothesized sodium channel cooperativity in some neurons that increases the rapidity relative to the Hodgkin-Huxley model, which may be responsible for the difference in dynamics of hippocampal and cortical neuron APs observed in this set. It would be useful to investigate sodium channel cooperativity in the hippocampus, and if data supporting that is different than in the cortex. In addition, FS neurons

show narrower APs, which suggests with faster potassium channel activation. There is little correlation between the rapidity and AP width values.

It can also be noted from Figure 5.5 that cortical neurons show a narrower range (lower standard deviation) of phase slope values than hippocampal neurons, suggesting that rapidity is consistent across FS and RS cortical neurons. This consistency suggests that this parameter is distinctly defined in cortical neurons, which may have implications for understanding the dynamics of sodium channel activation, both in cortical neurons and other regions of the brain by comparison.

Conclusions

AP rapidity is a valuable feature in machine learning algorithms for discriminating neuronal subtypes. This analysis suggests that including rapidity in machine learning algorithms greatly improves overall classification accuracy of these models. RS neurons are better discriminated by phase slope than other rapidity measures. The phase slope measure of rapidity shows the greatest ability to discriminate cortical from hippocampal neurons, with highly consistent values across subtypes of cortical neurons.

The results of this study indicate that machine learning is a highly effective tool for the classification of neuronal subtypes, and that the addition of rapidity to the classical parameters of AP width, AP amplitude, and AP onset greatly improves accuracy, with the majority of the classification capability in the rapidity and AP width features. Future work exploring these features in a greater number of neuronal subtypes may provide further insights into ion channel dynamics and differences among different neuron types.

6. Conclusions

MIC Device

Conclusions

Microfluidic Impedance Cytometry (MIC) has previously been shown as an effective tool for the classification and quantification of bacterial, yeast, and mammalian cells. This work provides a proof-of-concept for the use of MIC for parasite eggs, cysts, and oocysts on the scale of 50-100 μm in diameter. Improved understanding of MIC for the analysis of relatively large samples, such as various types of parasite eggs, would open doors for the use of MIC in a greater breadth of diagnostic applications. This work demonstrates the potential applicability of using an FPGA to function as lock-in amplifiers to improve sensitivity and simultaneously make multifrequency measurements from the same electrode set on a MIC device. The FPGA potentially provides a low-cost and customizable platform for numerous research applications. Measurements from 2 sets of electrodes allowed for the determination of the velocity of individual beads, as well as provided previously undescribed cross-set impedance measurements across the diagonal plane between each top electrode and its neighboring bottom electrode. The channel and electrode dimensions used for this work provide a foundation for future research using parasite egg samples. The FPGA setup provides a customizable platform for multifrequency measurements and optimization of frequencies.

Based on the ImageJ analysis of the salt, sieve, and gold standard methods, it was also concluded that the salt-based method resulted in smaller particle size, which is more ideal for use in microfluidic channels. Though the salt method had a greater number of particles and larger percentage of small particles, this method had significantly smaller particles. It is advised to use

this method when preparing samples for use with microfluidic devices to prevent clogging of the microchannel.

Suggested Future Work

Future applications for this work include multifrequency MIC of parasite eggs to examine internal structure for classification of different egg types. The use of laser-cut pressure-sensitive adhesive as the channel sidewalls between two electrode-patterned glass slides provides a low-cost method for fabrication, though there are inherent drawbacks. The rough edges of the channel sidewalls can increase clogging of the channel. It is advised to use laser-cut channels with optimized egg isolation protocols for rapid prototyping and reduced clogging of channels. In addition, the FPGA setup provides customizable frequencies and configurations. Based on the results from this research, the next suggested steps would be to test this device using egg isolation samples of strongyle eggs with the FPGA set up as two lock-in amplifiers. Future work can examine a broader range of egg types and frequencies. It is advised to optimize frequencies for one egg type, then begin at those frequencies when testing new egg types. The data collected from these different frequencies and different egg types can then be used to train a machine learning algorithm, such as k-nearest neighbors, with various combinations of frequencies as features, which can be used to determine the optimal frequencies for discriminating each egg type in a sample containing different combinations of egg types.

Neuron classification

Conclusions

The neuron classification work shows that kNN is the best classifier for this data set, though decision tree and SVM classifiers show promising results as well and should not be discounted when analyzing other data sets. The classification results show that AP rapidity is a valuable feature in machine learning algorithms for discriminating neuronal subtypes. The addition of any

measure of rapidity ($IFWd^2$, $IHWd^2$, or phase slope) to the classical feature set (AP width, AP amplitude, AP onset potential) greatly improves classification, with weighted f1-scores using the kNN classifier increasing from 0.954783 $\pm$ 0.003913 for classical features only, to 0.998035 $\pm$ 0.000097 for $IFWd^2$, 0.997330 $\pm$ 0.001115 for $IHWd^2$, and 0.999941 $\pm$ 0.000168 for phase slope. These results show that the rapidity feature adds information to the model that is not contained in the classical features and should be considered as a valuable attribute for future models.

Of the rapidity measures, phase slope showed the most accurate results for all of the classifiers, with nearly perfect classification (weighted f1-score of 0.999941 $\pm$ 0.000168) when used as a kNN feature along with the classical features. Using phase slope and width alone as kNN features produced a weighted f1-score of 0.999636 $\pm$ 0.000382. This shows that the addition of AP amplitude and onset potential do not provide substantial additional information for classification. In addition, comparing the weighted f1-score of classical features alone (0.954783 $\pm$ 0.003913) to the weighted f1-score of phase slope + width (0.999636 $\pm$ 0.000382), effectively replacing AP amplitude and onset potential with phase slope, shows that phase slope is more valuable for classification that both of these parameters combined. These conclusions suggest that the differences in APs generated by RS or FS cortical or hippocampal cells are more distinct based on phase slope and width, which may translate to differences in ion channel dynamics in these cell types and regions. Further exploration of classification using phase slope and width alone could provide insights into these dynamics in these types of cells as well as in other neuronal subtypes.

The weighted f1-scores in this work show large improvements from previous work (Ghaderi et al., 2018; Wang et al., 2022). Ghaderi et al. showed classification accuracy of 82.29 $\pm$ 1.31% using *in vivo* recordings of 3 neuronal subtypes and 84.13 $\pm$ 0.81% accuracy in *in vitro* recordings of 5 neuronal subtypes using discrete cosine transform, principal component analysis,

and c-means clustering. Wang et al. showed 88.76% accuracy for discrimination of 5 neuron subtypes using a convolutional neural network. The results from this work show drastically greater classification of 4 neuronal subtypes, with f1-scores for classical features and rapidity, and for AP width and phase slope, exceeding 0.999. Classical features plus any measure of rapidity also produced weighted f1-scores $\geq$ 0.99, which is still far greater than the results from previous studies. These findings suggest that rapidity, most notably phase slope, is an important feature for classification and the use of phase slope and width as kNN features produces more reliable and accurate results when compared to using two principal components from frequency domain transforms.

Suggested Future Work

The analysis of this dataset and the conclusions drawn open the door for further validation and expansion upon these results. Due to the limited dataset, this work was confined to four types of neurons, from two regions of the brain. These groups were chosen based of firing frequency (regular-spiking or fast-spiking) and brain region (hippocampus or cortex), though some of these neurons could be further sub-categorized. Future analysis on these subcategories could reveal underlying trends. These analyses would benefit from the inclusion of additional data from each of the subsets, as numbers of these subtypes contained in the set used in this work are insufficient to make strong generalizations. The addition of data from different sources would be beneficial to account for possible experimental biases and provide further validation for the trends observed between cortical and hippocampal data, which came from two different repositories.

Another experiment for further validation would be to perform knn analysis of the same feature sets using a different data (from different databases) with the same neuronal subtypes and

compare trends from this work to validate findings. Knn analysis could also be performed using the same feature sets, using data from additional different neuronal subtypes.

Based on the width vs. phase slope plots, further analysis tracing AP number within each spike train (multi-AP response to single stimulus/excitation pulse) and within each recording (all APs from one neuron over all pulses) could provide insights into single neuron behavior over time. Analysis could include adding data columns/features that include the AP number within the recording and the AP number within the spike train. These could then be plotted to show APs from certain points in the recording or the spike train. For example, the first spikes from each spike train could be compared to each other, reducing potential drift caused by "tiring" of the neuron.

References

Aldohbeyb, A.A., Vigh, J., Lear, K.L., 2021. New methods for quantifying rapidity of action potential onset differentiate neuron types. PLOS ONE 16, e0247242. https://doi.org/10.1371/journal.pone.0247242

Armañanzas, R., Ascoli, G.A., 2015. Towards Automatic Classification of Neurons. Trends Neurosci. 38, 307–318. https://doi.org/10.1016/j.tins.2015.02.004

Baiak, B.H.B., Lehnen, C.R., da Rocha, R.A., 2018. Anthelmintic resistance in cattle: A systematic review and meta-analysis. Livest. Sci. 217, 127–135. https://doi.org/10.1016/j.livsci.2018.09.022

Bean, B.P., 2007. The action potential in mammalian central neurons. Nat. Rev. Neurosci. 8, 451–465. https://doi.org/10.1038/nrn2148

Buccino, A.P., Ness, T.V., Einevoll, G.T., Cauwenberghs, G., Hafliger, P.D., 2018. A Deep Learning Approach for the Classification of Neuronal Cell Types. Annu. Int. Conf. IEEE Eng. Med. Biol. Soc. IEEE Eng. Med. Biol. Soc. Annu. Int. Conf. 2018, 999–1002. https://doi.org/10.1109/EMBC.2018.8512498

CDC - Parasites [WWW Document], 2022. URL https://www.cdc.gov/parasites/index.html (accessed 8.21.21).

Chen, J., Xue, C., Zhao, Y., Chen, D., Wu, M.-H., Wang, J., 2015. Microfluidic Impedance Flow Cytometry Enabling High-Throughput Single-Cell Electrical Property Characterization. Int. J. Mol. Sci. 16, 9804–9830. https://doi.org/10.3390/ijms16059804

Cheung, K., Gawad, S., Renaud, P., 2005. Impedance spectroscopy flow cytometry: On-chip label-free cell differentiation. Cytometry A 65A, 124–132. https://doi.org/10.1002/cyto.a.20141

Clark, C.A., Gunn, P.J., Dedrickson, J., Sorenson, J., 2014. Effects of Internal Parasite Infection at Feedlot Arrival on Performance and Carcass Characteristics in Beef Steers (No. 5087608). Iowa State University, Digital Repository, Ames. https://doi.org/10.31274/ans_air-180814-1146

Clatot, J., Hoshi, M., Wan, X., Liu, H., Jain, A., Shinlapawittayatorn, K., Marionneau, C., Ficker, E., Ha, T., Deschênes, I., 2017. Voltage-gated sodium channels assemble and gate as dimers. Nat. Commun. 8, 2077. https://doi.org/10.1038/s41467-017-02262-0

Clausen, C.H., Dimaki, M., Bertelsen, C.V., Skands, G.E., Rodriguez-Trujillo, R., Thomsen, J.D., Svendsen, W.E., 2018. Bacteria Detection and Differentiation Using Impedance Flow Cytometry. Sensors 18, 3496. https://doi.org/10.3390/s18103496

COMBAR, Combatting Anthelmintic Resistance in Ruminants, 2021. Faecal egg count reduction test (FECRT) protocol Gastrointestinal nematodes - CATTLE.

Conde, M.H., Heckler, R.P., Borges, D.G.L., Onselen, V.J.V., Brumatti, R.C., Borges, F. de A., 2019. Economic analysis of strategic control program (5, 8, 11) for gastrointestinal nematodes in grazing beef cattle during the growing phase in Central Brazil. Semina Ciênc. Agrár. 40, 2309. https://doi.org/10.5433/1679-0359.2019v40n5Supl1p2309

Cringoli, G., Rinaldi, L., Maurelli, M.P., Utzinger, J., 2010. FLOTAC: new multivalent techniques for qualitative and quantitative copromicroscopic diagnosis of parasites in animals and humans. Nat. Protoc. 5, 503–515. https://doi.org/10.1038/nprot.2009.235

da Silva Lantyer, A., Calcini, N., Bijlsma, A., Kole, K., Emmelkamp, M., Peeters, M., Scheenen, W.J.J., Zeldenrust, F., Celikel, T., 2018. A databank for intracellular electrophysiological mapping of the adult somatosensory cortex. GigaScience 7. https://doi.org/10.1093/gigascience/giy147

Dixon, R.E., Navedo, M.F., Binder, M.D., Santana, L.F., 2022. Mechanisms and physiological implications of cooperative gating of clustered ion channels. Physiol. Rev. https://doi.org/10.1152/physrev.00022.2021

Foreyt, W.J., 1989. Diagnostic Parasitology. Vet. Clin. North Am. Small Anim. Pract. 19, 979–1000. https://doi.org/10.1016/S0195-5616(89)50107-4

Gasbarre, L.C., 2014. Anthelmintic resistance in cattle nematodes in the US. Vet. Parasitol. 204, 3–11. https://doi.org/10.1016/j.vetpar.2014.03.017

Gawad, S., Cheung, K., Seger, U., Bertsch, A., Renaud, P., 2004. Dielectric spectroscopy in a micromachined flow cytometer: theoretical and practical considerations. Lab. Chip 4, 241. https://doi.org/10.1039/b313761a

Ghaderi, P., Marateb, H.R., Safari, M.-S., 2018. Electrophysiological Profiling of Neocortical Neural Subtypes: A Semi-Supervised Method Applied to in vivo Whole-Cell Patch-Clamp Data. Front. Neurosci. 12.

Gouwens, N.W., Sorensen, S.A., Berg, J., Lee, C., Jarsky, T., Ting, J., Sunkin, S.M., Feng, D., Anastassiou, C.A., Barkan, E., Bickley, K., Blesie, N., Braun, T., Brouner, K., Budzillo, A., Caldejon, S., Casper, T., Castelli, D., Chong, P., Crichton, K., Cuhaciyan, C., Daigle, T.L., Dalley, R., Dee, N., Desta, T., Ding, S.-L., Dingman, S., Doperalski, A., Dotson, N., Egdorf, T., Fisher, M., de Frates, R.A., Garren, E., Garwood, M., Gary, A., Gaudreault, N., Godfrey, K., Gorham, M., Gu, H., Habel, C., Hadley, K., Harrington, J., Harris, J.A., Henry, A., Hill, D., Josephsen, S., Kebede, S., Kim, L., Kroll, M., Lee, B., Lemon, T., Link, K.E., Liu, X., Long, B., Mann, R., McGraw, M., Mihalas, S., Mukora, A., Murphy, G.J., Ng, Lindsay, Ngo, K., Nguyen, T.N., Nicovich, P.R., Oldre, A., Park, D., Parry, S., Perkins, J., Potekhina, L., Reid, D., Robertson, M., Sandman, D., Schroedter, M., Slaughterbeck, C., Soler-Llavina, G., Sulc, J., Szafer, A., Tasic, B., Taskin, N., Teeter, C., Thatra, N., Tung, H., Wakeman, W., Williams, G., Young, R., Zhou, Z., Farrell, C., Peng, H., Hawrylycz, M.J., Lein, E., Ng, Lydia, Arkhipov, A., Bernard, A., Phillips, J.W., Zeng, H., Koch, C., 2019. Classification of electrophysiological and morphological neuron types in the mouse visual cortex. Nat. Neurosci. 22, 1182–1195. https://doi.org/10.1038/s41593-019-0417-0

Graham, M., 2003. The Coulter principle: foundation of an industry. J. Assoc. Lab. Autom. 8, 72–81. https://doi.org/10.1016/S1535-5535(03)00023-6

Gutkin, B., Ermentrout, G.B., 2006. Spikes too kinky in the cortex? Nature 440, 999–1000. https://doi.org/10.1038/440999a

Hodgkin, A.L., Huxley, A.F., 1952. A quantitative description of membrane current and its application to conduction and excitation in nerve. J. Physiol. 117, 500–544. https://doi.org/10.1113/jphysiol.1952.sp004764

Huang, M., Volgushev, M., Wolf, F., 2012. A Small Fraction of Strongly Cooperative Sodium Channels Boosts Neuronal Encoding of High Frequencies. PLOS ONE 7, e37629. https://doi.org/10.1371/journal.pone.0037629

Ilin, V., Malyshev, A., Wolf, F., Volgushev, M., 2013. Fast computations in cortical ensembles require rapid initiation of action potentials. J. Neurosci. Off. J. Soc. Neurosci. 33, 2281–2292. https://doi.org/10.1523/JNEUROSCI.0771-12.2013

Lee, S.-H., Marchionni, I., Bezaire, M., Varga, C., Danielson, N., Lovett-Barron, M., Losonczy, A., Soltesz, I., 2014. Parvalbumin-Positive Basket Cells Differentiate among Hippocampal Pyramidal Cells. Neuron 82, 1129–1144. https://doi.org/10.1016/j.neuron.2014.03.034

Levecke, B., Behnke, J.M., Ajjampur, S.S.R., Albonico, M., Ame, S.M., Charlier, J., Geiger, S.M., Hoa, N.T.V., Kamwa Ngassam, R.I., Kotze, A.C., McCarthy, J.S., Montresor, A., Periago, M.V., Roy, S., Tchuem Tchuenté, L.-A., Thach, D.T.C., Vercruysse, J., 2011. A Comparison of the Sensitivity and Fecal Egg Counts of the McMaster Egg Counting and Kato-Katz Thick Smear Methods for Soil-Transmitted Helminths. PLoS Negl. Trop. Dis. 5, e1201. https://doi.org/10.1371/journal.pntd.0001201

McGrath, J.S., Honrado, C., Spencer, D., Horton, B., Bridle, H.L., Morgan, H., 2017. Analysis of Parasitic Protozoa at the Single-cell Level using Microfluidic Impedance Cytometry. Sci. Rep. 7, 2601. https://doi.org/10.1038/s41598-017-02715-y

Naundorf, B., Wolf, F., Volgushev, M., 2006. Unique features of action potential initiation in cortical neurons. Nature 440, 1060–1063. https://doi.org/10.1038/nature04610

Parasites [WWW Document], 2018. . Cent. Dis. Control Prev. URL https://www.cdc.gov/parasites/index.html

Scare, J.A., Slusarewicz, P., Noel, M.L., Wielgus, K.M., Nielsen, M.K., 2017. Evaluation of accuracy and precision of a smartphone based automated parasite egg counting system in comparison to the McMaster and Mini-FLOTAC methods. Vet. Parasitol. 247, 85–92. https://doi.org/10.1016/j.vetpar.2017.10.005

Schindelin, J., Arganda-Carreras, I., Frise, E., Kaynig, V., Longair, M., Pietzsch, T., Preibisch, S., Rueden, C., Saalfeld, S., Schmid, B., Tinevez, J.-Y., White, D.J., Hartenstein, V., Eliceiri, K., Tomancak, P., Cardona, A., 2012. Fiji: an open-source platform for biological-image analysis. Nat. Methods 9, 676–682. https://doi.org/10.1038/nmeth.2019

Sun, T., Morgan, H., 2010. Single-cell microfluidic impedance cytometry: a review. Microfluid. Nanofluidics 8, 423–443. https://doi.org/10.1007/s10404-010-0580-9

Sutherland, I.A., Leathwick, D.M., 2011. Anthelmintic resistance in nematode parasites of cattle: a global issue? Trends Parasitol. 27, 176–181. https://doi.org/10.1016/j.pt.2010.11.008

Telenczuk, M., Fontaine, B., Brette, R., 2017. The basis of sharp spike onset in standard biophysical models. PLOS ONE 12, e0175362. https://doi.org/10.1371/journal.pone.0175362

Teleńczuk, M.T., Stimberg, M., Brette, R., 2015. Origin of the kink of somatic action potentials. BMC Neurosci. 16, O8. https://doi.org/10.1186/1471-2202-16-S1-O8

Utzinger, J., Rinaldi, L., Lohourignon, L.K., Rohner, F., Zimmermann, M.B., Tschannen, A.B., N'Goran, E.K., Cringoli, G., 2008. FLOTAC: a new sensitive technique for the diagnosis of hookworm infections in humans. Trans. R. Soc. Trop. Med. Hyg. 102, 84–90. https://doi.org/10.1016/j.trstmh.2007.09.009

Venkatesan, K., Liu, Y., Goldfarb, M., 2014. Fast-onset long-term open-state block of sodium channels by A-type FHFs mediates classical spike accommodation in hippocampal pyramidal neurons. J. Neurosci. Off. J. Soc. Neurosci. 34, 16126–16139. https://doi.org/10.1523/JNEUROSCI.1271-14.2014

Wang, R., Han, S.M., Gajowa, M., Liu, C., 2022. NEOCORTICAL CELL TYPE CLASSIFICATION FROM ELECTROPHYSIOLOGY RECORDINGS USING DEEP NEU- RAL NETWORKS 11.

Wilson, J.W., Park, J.K., Warren, W.S., Fischer, M.C., 2015. Flexible digital signal processing architecture for narrowband and spread-spectrum lock-in detection in multiphoton microscopy and time-resolved spectroscopy. Rev. Sci. Instrum. 86, 033707. https://doi.org/10.1063/1.4916261

Appendices

Appendix A: Correlation Matrix Data Mining for AP Analysis

The correlation matrix, above, shows highly correlated (|coefficient| > 0.5) values in bold and highly uncorrelated values highlighted in yellow. To determine the best features to use for discrimination of the neuronal subtypes (labels), it is beneficial to look at features that are highly correlated with labels, as well as feature combinations that are highly uncorrelated, as these features will provide different information.

It can be noted that the AP Width is highly correlated with both of the cortical neuron subtypes, and that the rapidity features are highly correlated with the hippocampal subtypes. Given that the phase slope rapidity measure shows higher correlation with hRS that the second derivative methods show with hFS, it can be hypothesized that using AP Width alongside phase slope will show an accurate classification of cRS, cFS, and hRS neuronal subtypes. Additionally, the values with low correlation, shown in yellow, indicate that these parameters do not contain similar information, and therefore these combinations of features should be examined further.

Table A1: Correlation Matrix of AP Features and Neuron Labels

	AP Onset (mV)	**AP Amplitude (mV)**	**AP Width (ms)**	**IFWd2 (1/ms)**	**IHWd2 (1/ms)**	**Phase Slope (1/ms)**	**hRS**	**hFS**	**cRS**	**cFS**
AP Onset (mV)	1.000000	-0.179263	0.513569	-0.122950	-0.084237	-0.022614	0.104203	-0.013822	-0.405257	0.314817
AP Amplitude (mV)	-0.179263	1.000000	0.265098	-0.005700	-0.057265	0.284538	0.301751	-0.350373	-0.334552	0.259959
AP Width (ms)	***0.513569***	0.265098	1.000000	-0.422154	-0.371015	-0.063992	0.245197	-0.451130	-0.625536	0.653815
IFWd2 (1/ms)	-0.122950	-0.005700	-0.422154	1.000000	0.974980	0.657809	0.408668	0.730461	-0.279003	-0.499940
IHWd2 (1/ms)	-0.084237	-0.057265	-0.371015	***0.974980***	1.000000	0.607583	0.344635	0.746148	-0.307642	-0.423777
Phase Slope (1/ms)	-0.022614	0.284538	-0.063992	***0.657809***	***0.607583***	1.000000	0.791930	0.187719	-0.379792	-0.434055
hRS	0.104203	0.301751	0.245197	0.408668	0.344635	**0.791930**	1.000000	-0.162429	-0.391195	-0.409640
hFS	-0.013822	-0.350373	-0.451130	**0.730461**	**0.746148**	0.187719	-0.162429	1.000000	-0.206914	-0.216670
cRS	-0.405257	-0.334552	**-0.625536**	-0.279003	-0.307642	-0.379792	-0.391195	-0.206914	1.000000	-0.521828
cFS	0.314817	0.259959	**0.653815**	-0.499940	-0.423777	-0.434055	-0.409640	-0.216670	-0.521828	1.000000

Appendix B: Optimization of k in k-nearest neighbors

To optimize the value of k for k-nearest neighbors, the k value was varied from 1 to 20, and scored using the macro f1-score value. Though k=1 had the highest value for both of the second derivative methods, using a k value of 1 will likely lead to over-fitting, so this value was discarded. A k value of 3 was used for all of the feature sets, as it showed the highest score for the classical set and the classical + phase slope sets, and the second highest for both of the second derivative sets. It can be noted that the f-score also increases from k=4 to k=5, but not as high as k=3, so k=5 may also be considered, as it may provide better classification in a larger data set. Though these observations show which values of k are more optimal, it can be generally noted that classification is not highly influenced by the k-value.

Table B1: Macro f1-scores for k-nearest neighbors analysis with varying k values

k	Classical	IFWd2	IHWd2	Phase Slope
1	0.9594265653368446	0.9985386534528324	0.9978119630977189	0.9999968442292546
2	0.9539307062910506	0.9980792738321675	0.9973098508850365	0.9999804986293266
3	0.960284232667355	0.9984026000850953	0.9976082303272201	0.9999804986293266
4	0.957820965162337	0.997845630247469	0.9970266447224381	0.9998973058915985
5	0.9599826093575993	0.9979062266860939	0.9970837314798103	0.9998973058915985
6	0.9583179407184949	0.9974418384467153	0.9966093808000911	0.9997400029221285
7	0.9592617257122577	0.9975059699891113	0.9965860161928725	0.9997374022017117
8	0.9581903844840218	0.9970353721598713	0.995942797672789	0.9997244017895464
9	0.958874577324262	0.9970686818760285	0.9959918863363453	0.9997179002334355
10	0.9579337724497187	0.9966168111898546	0.9952892905165065	0.9997033220322998
11	0.9574997918716593	0.9966770171389433	0.9953339331673015	0.9996866998415769
12	0.9565788943504465	0.9961206855365383	0.9945731419979397	0.9996656198921589
13	0.9562570747391858	0.9961163608138078	0.9946459036984274	0.9996242963516847
14	0.9554891548284886	0.9954344519865181	0.9939097853887744	0.9996227194427082
15	0.9551184871292957	0.9954591257422676	0.9939369875270373	0.9995488932009764
16	0.9545340454951238	0.9948943883440639	0.9931820420988513	0.9995553945978423
17	0.954268725706808	0.9949028913877809	0.9932891674357583	0.9995111901681774
18	0.9537234803766633	0.9944537660756894	0.9924954970424671	0.9995018132894312
19	0.9532273337457968	0.9945367155127692	0.9926779180306046	0.9994511068037785
20	0.9527767501853689	0.9940518752074602	0.9918531156179827	0.9994476707459171

Appendix C: List of co-authored publications and presentations resulting from doctorate work

Publications:

1. W Tedjo*, **JE Nejad***, RM Feeny, L Yang, CS Henry, S Tobet, and T Chen. Electrochemical Biosensor System Using a CMOS Microelectrode Array Provides High Spatially and Temporally Resolved Images. *Biosensors and Bioelectronics*. April 2018. *Co-first authors

2. **J.E. Nejad**, A.C. Mugdha, J.W. Wilson, A.K. McGrew, and K.L. Lear, "Multifrequency Microfluidic Impedance Cytometer Using a Field-Programmable Gate Array for Parasite Egg Analysis", Proceedings of the *Rocky Mountain Bioengineering Symposium* (also published in *Biomedical Sciences Instrumentation*), vol. 56, pp. 184-191, April 2020.

3. L.M. Abburi, **J.E. Nejad**, and K.L. Lear, "Solder Mask as a Microfluidic Channel Wall for Electrical Impedance Measurements on Printed Circuit Boards", Proceedings of the *Rocky Mountain Bioengineering Symposium* (also published in *Biomedical Sciences Instrumentation*), vol. 56, pp. 192-200, April 2020.

4. M.M. Koepke, **J.E. Nejad**, and K.L. Lear, "Optical Trigger for Parasite Egg Microfluidic Impedance Cytometry Measurements", Proceedings of the *Rocky Mountain Bioengineering Symposium* (also published in *Biomedical Sciences Instrumentation*), vol. 56, pp. 219-226, April 2020.

5. N Ramo, **J.E. Nejad**, K Popat, and K Catton. Student Assessment of Active Learning Elements in 100-level Introductory Biomedical Engineering Course. 2018 *American Society for Engineering Education (ASEE) Annual Conference Proceedings*. June 2018.

Conference Poster Presentations:

1. J.E. Nejad, L.M. Abburi, J.R. Cerda, E.A. McDermott, A.K. McGrew, and K.L. Lear. “Towards Automated Identification and Enumeration of Eggs in Fecal Samples”, *American Association of Veterinary Parasitologists Annual Meeting*, Lexington, KY, June 2021.

2. J.E. Nejad, A.K. McGrew, K.L. Lear. “Multifrequency Microfluidic Impedance Cytometry for Parasitology” *Biomedical Engineering Society Conference,* 2020,

3. J.E. Nejad, A.K. McGrew, K.L. Lear. “Initial Considerations for the Use of Microfluidic Impedance Cytometry for Fecal Egg Count Automation and Classification." *Rocky Mountain Conference of Parasitologists.* Sep 2019.

4. J.E. Nejad, A.K. McGrew, K.L. Lear. “Microfluidic Biosensor System for Parasite Diagnostics.” *Graduate Student Showcase, Colorado State University*. Nov 2019.

5. J.E. Nejad, A.K. McGrew, K.L. Lear. “Calibration of a High-Density Microelectrode Array for Improved Spatiotemporal Resolution in an Electrochemical Biosensor” *Front Range Computational and Systems Biology Symposium: Sensing and Sequencing Microbes,* July 2016, Fort Collins.

6. J.E. Nejad, W.Tedjo, T. Chen "An Electrochemical Biosensor System for Chemical Imaging of Live Biological Samples with High Spatiotemporal Resolution."*Biomedical Engineering Society (BMES) Conference*, Oct 2017, Phoenix, AZ

7. J.E. Nejad, W.Tedjo, R. Feeny, C. Henry, T. Chen “Electrochemical Imaging of Neurotransmitter Gradients *in Live Tissue using a CMOS Microelectrode Array.” GAUSSI Symposium*, June 2017, Fort Collins, CO.